RSC Advances

PAPER

View Article Online
View Journal | View Issue

Check for updates

Cite this: *RSC Adv.*, 2025, **15**, 13662

Ultrasound-assisted synthesis of biomass-derived carbon-supported binary metal oxides for efficient adsorption of heavy metals from wastewater†

Walaa S. Gado,[a] Asmaa S. Morshedy,[a] Ahmed M. Masoud,[b] Ard elshifa M. E. Mohammed,[c] Entsar H. Taha,[d] Adel A. El-Zahhar,[e] Majed M. Alghamdi,[e] Ahmed M. A. El Naggar*[a] and Esraa M. El-Fawal[a]

Received 3rd January 2025
Accepted 5th March 2025

DOI: 10.1039/d5ra00057b

rsc.li/rsc-advances

Heavy metal contamination in water sources remains a critical environmental issue, primarily due to industrial activities, in terms of its continuous contribution to pollution through non-compliance and illegal discharge. This study presents an innovative biochar-supported binary metal oxide composite (nickel oxide (NiO) and cobalt oxide (CoO) nanoparticles) synthesized *via* ultrasound-assisted techniques for efficient adsorption of Zn(II) and Cd(II) ions from wastewater. By utilizing solid residues and leveraging ultrasound technology, this approach aligns with the principles of green chemistry due to utilization of a renewable biomass-based source, enhancing energy efficiency in the synthesis process, and minimizing waste production. Thereby a sustainable and innovative route for material development is explicitly demonstrated. Structural and morphological characterizations confirm the uniform integration of Nickel oxide (NiO) and cobalt oxide (CoO) particles into the biochar matrix, leading to maximum adsorption capacities of 18.9 mg g^{-1} for Zn(II) and 10.2 mg g^{-1} for Cd(II). The adsorption process follows a chemisorptive monolayer mechanism, as demonstrated by kinetic and isotherm studies, and is thermodynamically confirmed to be endothermic and spontaneous. The material also exhibits excellent reusability over five adsorption–desorption cycles. By integrating sustainable resources with innovative synthesis techniques, this work contributes to advancing wastewater remediation technologies while supporting global sustainability initiatives.

1. Introduction

Heavy metal pollution in aquatic environments has emerged as a global environmental challenge due to the extensive industrial use of metals like cadmium (Cd), zinc (Zn), nickel (Ni), and copper (Cu).[1–3] These pollutants are non-biodegradable, toxic, and prone to bioaccumulation, threatening aquatic ecosystems, soil fertility, and human health.[4,5] The World Health Organization (WHO) and other regulatory bodies have set stringent limits for these metals in water to mitigate their adverse effects—for instance, the permissible levels for zinc and cadmium in drinking water are 3 mg L^{-1} and 0.003 mg L^{-1}, respectively.[6,7] Industrial processes, including metal plating, pigment production, and battery manufacturing, discharge heavy metals into water bodies, exacerbating contamination levels.[8–10] Addressing this issue requires the development of innovative and sustainable technologies that align with the principles of green chemistry.

Traditional methods for heavy metal removal, such as chemical precipitation,[11] ion exchange,[12] membrane separation,[13] solvent extraction,[14] often face limitations related to cost, efficiency, and secondary waste generation. For instance, chemical precipitation can generate large volumes of sludge, requiring additional treatment and disposal, which increases operational costs. Ion exchange, while effective, is often expensive due to the high cost of resins and their regeneration. Membrane separation, although efficient, is energy-intensive and prone to fouling, leading to increased maintenance costs. Solvent extraction, on the other hand, can produce toxic organic solvents as byproducts, posing environmental risks.[11–15] Adsorption has emerged as a preferred approach due to its cost-effectiveness, high efficiency, and adaptability to renewable materials.[15–19] However, the search for advanced adsorbents that are both scalable and environmentally friendly remains a crucial area of research. Recent advances in materials science

---

[a] *Egyptian Petroleum Research Institute (EPRI), Nasr City, 11727, Cairo, Egypt*
[b] *Nuclear Materials Authority, P.O. Box 530, El Maadi, Cairo, Egypt*
[c] *Department of Chemistry, College of Science, Qassim University, Al-Qassim, Saudi Arabia*
[d] *Department of Plant Protection, Faculty of Agriculture, Ain Shams University, Egypt*
[e] *Department of Chemistry, Faculty of Science, King Khalid University, Abha 9004, Saudi Arabia. E-mail: drmeto1979@yahoo.com*

† Electronic supplementary information (ESI) available: Additional experimental details, mathematical models, and relevant supporting figures or tables referenced in the manuscript. See DOI: **https://doi.org/10.1039/d5ra00057b**

offer the potential to overcome these challenges by integrating renewable resources with innovative synthesis techniques.

Solid agricultural waste has emerged as a promising resource for addressing environmental and sustainability challenges.[20–22] Materials such as crop residues, fruit peels, and other biomass are often discarded as waste, contributing to environmental degradation.[20–22] However, these resources can be transformed into value-added materials like bio-char, which possess unique physicochemical properties suitable for environmental applications.[23,24] Utilizing agricultural waste for bio-char production not only mitigates waste disposal issues but also aligns with the circular economy model by creating sustainable materials for advanced technologies.[20–24]

This study presents an innovative approach to heavy metal adsorption through the synthesis of a bio-char-supported binary metal oxide composite (nickel oxide (NiO) and cobalt oxide (CoO) nanoparticles). Nickel oxide (NiO) and cobalt oxide (CoO) were selected due to their well-documented high surface area, stability, and strong affinity for metal ion adsorption. NiO is known for its excellent catalytic and adsorptive properties, while CoO enhances redox interactions, improving adsorption kinetics. Their combined use creates a synergistic effect, optimizing adsorption performance. Additionally, both oxides demonstrate structural compatibility with biochar, ensuring homogeneous dispersion and maximizing active sites for heavy metal uptake. By utilizing pressed sunflower leaves as a renewable biomass source, bio-char was produced *via* pyrolysis and subsequently functionalized with nickel and cobalt oxides using ultrasonic homogenization. This method not only aligns with the principles of green chemistry by minimizing the use of synthetic materials but also leverages the transformative power of ultrasound technology to enhance material properties and performance. Comprehensive analyses, including adsorption kinetics, thermodynamics, and isotherm modeling, were performed for providing insights into the underlying mechanisms.

By integrating renewable resources with advanced synthesis methodologies, this study exemplifies the potential of chemistry to address pressing environmental challenges. The use of sunflower-derived bio-char underscores the importance of utilizing agricultural waste as a sustainable feedstock, while the ultrasonic-assisted synthesis emphasizes the role of innovative technologies in creating high-performance materials. These findings contribute not only to wastewater remediation but also to broader efforts in developing scalable, green, and effective solutions for environmental sustainability. This work underscores the transformative role of chemistry in achieving sustainable environmental solutions and providing a blueprint for designing next-generation adsorbents that are efficient, sustainable, and aligned with global efforts to mitigate pollution and protect natural resources.

2. Experimental

2.1. Materials

Analytical grades of chemical reagents were utilized in this study and all of them were used as-received with no further treatments. These chemicals including anhydrous zinc sulfate ($ZnSO_4$) and Cadmium sulfate ($CdSO_4$) were used to prepare a stock solution of cadmium and zinc ions using double-distilled water. Anhydrous nickel chloride ($NiCl_2$) and cobalt chloride ($CoCl_2$) were employed to synthesize the hydroxide structures of these metals. The previously mentioned reagents had a purity of 99.9% and they were purchased from Sigma-Aldrich, UK. Ammonia solution (NH_4OH 35%), obtained from ADWIC-Egypt, was used as a precipitator during the process of producing metal oxide species, passing firstly through the obtainment of their metal hydroxide species. Pressed sunflower leaves were presented in this study as a raw solid biomass residual for preparing activated biochar particles to be utilized as support for the two metal oxides, generating a binary oxide composite. Pure nitric, hydrochloric, and sulfuric acids (Merck, Germany) were used during the recovery of sorbents *via* the desorption of metal ions.

2.2. Synthesis of sorbent

The preparation of the introduced adsorbent in this research work was done through two consecutive steps. In the first one, bio-char species were prepared *via* pyrolysis of pressed sunflower residues at 300 °C under a nitrogen atmosphere for 2 hours. This temperature was chosen to ensure complete carbonization and enhance the porosity of the bio-char. The bio-char was thoroughly washed with deionized water and was then dried at 100 °C for 12 hours. It is important to note that no pretreatment was performed on the precursor material, as reported by Moniem *et al.*[23]

In the second step, Nickel oxide (NiO) and cobalt oxide (CoO) nanoparticles were synthesized using a co-precipitation method. Nickel chloride ($NiCl_2$) and cobalt nitrate ($Co(NO_3)_2$) solutions were mixed with ammonium hydroxide (NH_4OH) as a precipitating agent under continuous stirring, forming hydroxide precursors ($Ni(OH)_2$ and $Co(OH)_2$). These precursors were then calcined at 400 °C for 3 hours to yield NiO and CoO nanoparticles, as described by Ali *et al.*[24] The chemical reactions involved are as follows:

$$NiCl_2 + 2NH_4OH \rightarrow Ni(OH)_2 + 2NH_4Cl$$

$$Co(NO_3)_2 + 2NH_4OH \rightarrow Co(OH)_2 + 2NH_4NO_3$$

$$Ni(OH)_2 \xrightarrow{\Delta} NiO + H_2O$$

$$Co(OH)_2 \xrightarrow{\Delta} CoO + H_2O$$

Subsequently, the particles of metal oxides were coupled with the activated bio-char using ultrasonic waves, producing a composite adsorbent containing 20% of its weight as 50 : 50 of the two metal oxide particles. Particularly, calculated amounts of nickel oxide and cobalt oxide were suspended with a corresponding weight of the activated bio-char (representing 80% of the adsorbent composition) in a proper volume of ethanol under the effect of ultrasound waves for a time of 30 min using a homogenizer to ensure uniform distribution of the metal oxides within the activated bio-char matrix. The resulting composite was dried at 60 °C for 24 hours and stored for further characterization. The ultrasound-assisted synthesis method was employed to enhance the dispersion and interaction of NiO/CoO nanoparticles with biochar. The intense cavitation and microstreaming effects generated by ultrasound could facilitate uniform dispersion of metal oxides, prevented particle aggregation, and preserved the biochar's porous structure. These advantages are evident from the composite's homogeneous morphology (SEM), strong metal-support interactions (FTIR), and optimized adsorption performance. In contrast, conventional methods without ultrasound may lead to uneven metal oxide distribution, weaker binding, and reduced adsorption efficiency. The integration of ultrasound during synthesis procedures ensures superior composite properties and enhanced adsorption capacity, confirming its role in improving material functionality.

2.3. Sorbent characterization

To figure out morphological, structural and surface characteristics of the produced composite structures, several analytical tools were utilized. Details of the employed instruments for determination of such features are described in Section S1, see the provided ESI† with this article.

2.4. Adsorption experiments

Sorption tests were conducted to investigate the ability of CoO/NiO@bio-char to absorb Zn(II) and Cd(II) from an aqueous solution. Batch experiments were conducted using a Thermo-shaker water bath (Scientific Precision SWB 27, Waltham-USA) in a polypropylene tube. To conduct the experiments, a certain weight of sorbent (*m*, g) was added to a definite volume (*V*, L) of metal-containing aqueous solution (Co, 40 mg L^{-1}) and shaken for 240 minutes at room temperature (25 ± 1 °C). Regarding the investigation plan, solution pH from 2–8 and the sorbent dosage from 0.5 g L^{-1} to 4.0 g L^{-1} were examined.

For the desorption investigation, a similar experimental procedure was followed. The metal loading was done using the method mentioned earlier and the total metal present on the CoO/NiO@bio-char was calculated using the mass balance equation. Bimetal-loaded sorbents were mixed with a fixed volume of eluent (nitric acid, hydrochloric acid, or sulfuric acid) for 10 hours, with the sorbent dosage set at 3.0 g L^{-1}. After filtration, the concentration in the eluate was analyzed to calculate the amount released and to find out the desorption efficiency. The recycling process of the sorbent was studied for five consecutive cycles of adsorption and desorption. During this process, CoO/NiO@bio-char was mixed with an aqueous metal solution that contained 40 mg L^{-1} of Zn(II) and Cd(II). The sorbent dosage was 3.0 g L^{-1}, and the mixture was shaken for 4 hours at room temperature. The metal ions were then desorbed from the sorbent using a proper eluent with a sorbent dosage of 3.0 g L^{-1}. The suspension was kept under agitation for 4 hours at room temperature, and the solutions were mixed and analyzed to determine the cumulative desorption of target metals.

Adsorption kinetics were monitored by periodically sampling the supernatant at different time intervals (5–600 min) and a sorbent dosage of 3.0 g L^{-1}. The 4 hours equilibrium time was chosen based on preliminary studies indicating that adsorption rates stabilize after this period. The initial concentration interval of 20 to 120 mg L^{-1} was tested to explore the isotherm performance and evaluate the maximum capacity. Lagergren, pseudo-second-order, and intraparticle diffusion (Weber and Morris) kinetic equations were applied to describe the adsorption kinetic, while the uptake isotherm was modeled using Langmuir, Freundlich, Dubinin–Radushkevich (D–R), and Sips isotherm equations. The non-linear form of the applied kinetic and isotherm equations were declared in Table S1†.[25–30] The main idea of the models used is found in their respective references. The fitting of the applied kinetic and isotherm models is deduced based on the average relative error (ARE), and coordination coefficient (R^2) equations (Table S1†).[25–30] The thermodynamic performance of the uptake process was investigated at different reaction temperatures of 25–50 ± 1 °C. The thermodynamic parameters namely; standard Gibbs free energy change ($\Delta G°$), standard enthalpy change ($\Delta H°$), and standard entropy change ($\Delta S°$) were evaluated using equations listed in Table S1.†[31,32]

In all the experiments conducted, the initial concentration (Co, mg L^{-1}) and the final residual concentration (Ce, mg L^{-1}) of Zn(II) and Cd(II) were analyzed using Atomic Absorption Spectrometer GBC 932 AA (UK). Before the analysis, the samples were filtered through 0.22 mm filters. Each test was repeated three times, and only a relative error mean value of ≤5% was considered acceptable. The sorption efficiency (*E*%), sorption capacity (q_e, mg g^{-1}), and distribution coefficient (K_d) were calculated using eqn (1)–(3), as described in reference.

$$q_e = (C_o - C_e) \times \frac{V}{m} \tag{1}$$

$$R\% = \frac{(C_o - C_e)}{C_o} \times 100 \tag{2}$$

$$K_d = \frac{q_e}{C_e} \times \ 100 \tag{3}$$

3. Results & discussion

3.1. Sorbent characteristics

3.1.1. XRD patterns. The crystalline structure and phase composition of the biochar-based adsorbents were analyzed using X-ray diffraction (XRD). The XRD patterns (Fig. 1) of both the blank biochar and the NiO/CoO-modified composite exhibited a broad signal at $2\theta = 12°$, characteristic of amorphous carbon. A broader peak between 20° and 30° corresponds to the disordered carbon matrix within biochar, confirming its suitability as a porous support structure.[2,3] A peak at ∼40.17° was assigned to the (002) lattice plane of graphitic carbon, in

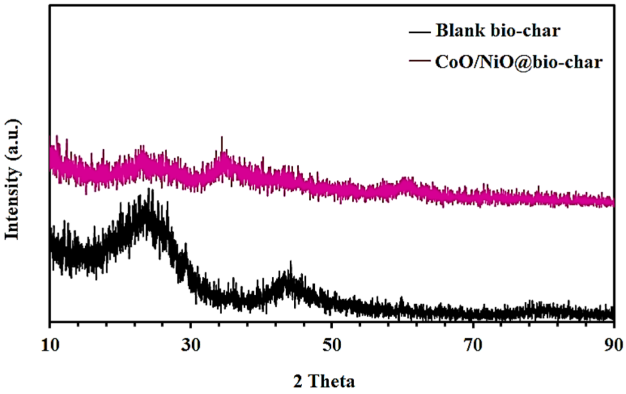

Fig. 1 XRD patterns of blank bio-char, and CoO/NiO@bio-char materials.

agreement with Ali *et al.*[24] The XRD patterns of the composite exhibited distinct peaks at $2\theta = 31.5°$ and 34.7°, corresponding to cobalt oxide (CoO),[33] and additional peaks at 33.4° and 36.9°, associated with nickel oxide (NiO).[34] These peaks confirm the successful incorporation of NiO and CoO nanoparticles into the biochar matrix.

Although biochar constitutes 80% of the composite, the notable alteration in its XRD signal is attributed to strong interactions between the biochar matrix and the embedded metal oxides. The incorporation of NiO and CoO modifies the local electronic structure, redistributing electron density across the carbon framework. Additionally, ultrasound-assisted dispersion promotes uniform metal oxide dispersion, influencing the overall crystalline arrangement of the composite. This interaction results in a reduction in the intensity of biochar-related peaks, primarily due to partial coverage of the carbon matrix by NiO and CoO nanoparticles and increased scattering effects from the crystalline metal oxide domains. Furthermore, the presence of highly disordered carbon regions, induced by metal oxide incorporation and ultrasonic treatment, contributes to the observed peak broadening and intensity variations. The absence of distinct X-ray diffraction (XRD) peaks corresponding to nickel (Ni) and cobalt (Co) in the composite can be attributed to several factors inherent to the material's characteristics and the limitations of the XRD technique. One primary reason is the nanocrystalline nature of the Ni and Co particles within the composite. When metal particles are reduced to the nanoscale, especially below 10 nm, their diffraction peaks tend to broaden significantly and decrease in intensity due to the effects of particle size on peak broadening. This phenomenon can render the peaks indistinguishable from the background noise, making them challenging to detect.

Additionally, if the Ni and Co particles are well-dispersed within an amorphous carbon matrix, their relative concentration might fall below the detection limit of the XRD instrument. XRD typically requires a minimum phase concentration—often around 4 weight percent—to produce discernible peaks. If the metal content is below this threshold, the corresponding peaks may not be observable. Furthermore, the formation of solid solutions or alloys between Ni and Co can lead to overlapping diffraction peaks, complicating the identification of individual metal phases. The similar crystal structures and lattice parameters of Ni and Co result in diffraction peaks occurring at nearly identical positions, causing them to merge and appear as a single broadened peak. This overlap can obscure the presence of distinct Ni and Co phases in the XRD pattern. The lack of clear Ni and Co peaks in the XRD analysis is likely due to the nanoscale size of the metal particles, their dispersion within the amorphous carbon matrix, potential low concentration below the detection limit, and the overlapping of diffraction peaks in the case of alloy formation. These factors collectively contribute to the challenges in detecting distinct Ni and Co phases using XRD in such composites.

Additional sharp peaks at higher angles ($2\theta = 42°$, 48°, and 75.6°) correspond to specific crystallographic planes, further confirming the successful integration of NiO and CoO into the biochar matrix.[33,34] To validate the crystalline phases, XRD analysis was referenced against standard JCPDS data, where NiO aligns with JCPDS Card No. 47-1049 and CoO matches JCPDS Card No. 48-1719. These results confirm the hybrid nature of the composite, demonstrating that the synergistic combination of biochar and metal oxides enhances adsorption capacity and chemical stability, making it a highly effective material for heavy metal removal applications.

3.1.2. FTIR spectra. Fourier-transform infrared (FTIR) spectroscopy was employed to identify functional groups critical for adsorption. The spectrum of the blank biochar displayed a broad absorption band at 3448 cm^{-1}, corresponding to O–H stretching vibrations from hydroxyl (–OH) and carboxyl (–COOH) groups (Fig. 2).[23,24] These functional groups play a key role in metal ion binding through electrostatic interactions and complexation. Additional vibrational bands in the 1500–1000 cm^{-1} region correspond to C–Cl, CH_2, and CH_3 groups, which contribute to the hydrophobic-hydrophilic balance of the adsorbent. In the NiO/CoO@biochar composite, FTIR peaks associated with biochar appear weakened or slightly shifted, indicating strong interactions between functional groups and the embedded metal oxides (Fig. 2). The presence of Ni–O and Co–O bonds, confirmed by additional bands in the 600–980 cm^{-1} region, suggests the formation of robust metal-biochar linkages that modify the local electronic structure of

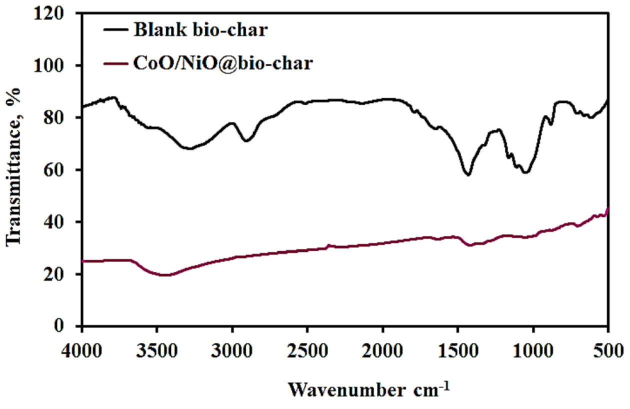

Fig. 2 FTIR spectra of both pure bio-char and CoO/NiO@bio-char.

the biochar. The reduction in hydroxyl (–OH) and carboxyl (–COOH) peak intensity is attributed to their partial coordination with NiO and CoO, which restricts their free vibrational modes and alters their spectral positions. Furthermore, ultrasound-assisted dispersion of metal oxides enhances their interaction with biochar, further influencing the composite's electronic structure and leading to slight spectral shifts. Additional FTIR peaks, characteristic of ortho- and para-substituted aromatic structures, are detected in the 600–980 cm^{-1} range for both the blank biochar and the composite, reflecting the presence of carbonaceous aromatic functionalities. The incorporation of NiO and CoO nanoparticles is further validated by distinct metal–oxygen (Ni–O and Co–O) stretching vibrations, confirming the successful integration of metal oxides into the biochar framework.[33,34]

3.1.3. Raman spectroscopy. Raman spectroscopy provided insights into the carbon structure of the adsorbents. Both samples exhibited two prominent peaks: the D-band at 1325 cm^{-1}, associated with disordered graphite-like structures, and the G-band at 1589 cm^{-1}, corresponding to sp^2-hybridized graphitic carbon domains (Fig. 3).[16,18] The significant changes observed in the Raman spectra of the NiO/CoO@biochar composite compared to blank biochar (Fig. 3) arise from strong electronic interactions between the metal oxides and the carbon matrix. The I_D/I_G ratio slightly increases in the composite, indicating a rise in structural disorder. This is likely due to the distortion of graphitic domains by NiO and CoO nanoparticles, which induce localized defects in the sp^2-hybridized carbon framework. Additionally, the broadening and decreased intensity of the G-band can be attributed to charge transfer effects between biochar and the embedded metal oxides, as well as the enhanced dispersion of NiO/CoO within the matrix, which disrupts graphitic ordering. The I_D/I_G ratio, a key measure of graphitization, was found to be 0.85, indicating a semi-ordered carbon structure—suggesting that while graphitization is present, the material is not fully crystalline graphite.[16,18] The coexistence of sp^2-hybridized graphitic domains with disordered regions confirms the composite's structural integrity, supporting its high stability and effective adsorption properties.[16,18]

3.1.4. SEM and EDX analyses. Scanning electron microscopy (SEM) revealed detailed morphological characteristics of the adsorbents (Fig. 4). The blank biochar displayed a predominantly smooth and porous structure, indicative of its potential for adsorptive applications. In contrast, the NiO/CoO@biochar composite exhibited a rougher surface morphology, which can be attributed to the agglomeration of nickel and cobalt oxide nanoparticles.[8–10] These nanoparticles were well-distributed across the biochar matrix, forming spherical, triangular, and tetrahedral structures with sizes ranging from a few nanometers to several microns. This morphological diversity enhances the composite's ability to interact with target ions, providing a large active surface area. Higher magnification SEM images revealed the presence of tube-like structures embedded within the biochar surface, which are likely formed by deep dispersion of metal oxides.[8–10] These features contribute to the composite's hierarchical porosity and support efficient diffusion of metal ions during adsorption processes.

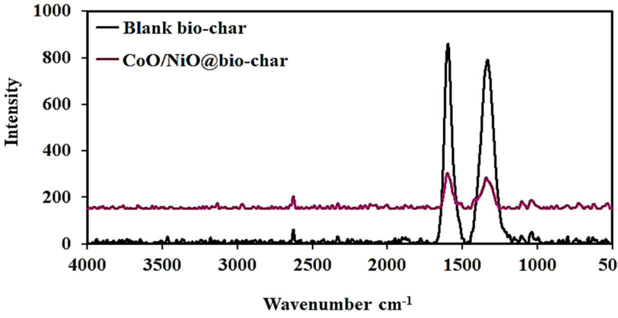

Fig. 3 Raman spectroscopy charts for both blank bio-char and CoO/NiO@bio-char.

Energy-dispersive X-ray (EDX) analysis further verified the elemental composition of the composite, detecting strong signals for carbon and oxygen—the principal components of the biochar—as well as nickel and cobalt, confirming the successful incorporation of metal oxides (Fig. 4). Quantitative analysis showed that biochar constituted approximately 80% of the composite's weight, while metal oxides accounted for the remaining 20%, consistent with the preparation protocol. The coexistence of organic and inorganic phases creates a heterogeneous surface, providing diverse active sites for heavy metal adsorption and enhancing the material's functional versatility.

3.1.5. Surface area analysis. The specific surface area and pore structure of the materials were thoroughly investigated using Brunauer–Emmett–Teller (BET) analysis. The blank biochar exhibited an impressively high specific surface area of 883.29 $m^2\ g^{-1}$, indicative of its highly porous structure and suitability for adsorption applications. In contrast, the NiO/CoO composite demonstrated a reduced specific surface area of 232.55 $m^2\ g^{-1}$, primarily due to the partial blockage of biochar pores by embedded metal oxide particles (Table 1).[8,24] Despite this reduction, the composite retained a mesoporous nature, with an average pore diameter of 3.31 nm, slightly larger than that of blank biochar (2.94 nm), reflecting structural modifications induced by metal oxide incorporation (Table 1). The nitrogen adsorption–desorption isotherm of NiO/CoO@biochar exhibits a type IV isotherm with an H3 hysteresis loop, indicating a dominantly mesoporous structure with flaky-shaped or interconnected pores. The discontinuity observed at the beginning and end of the desorption loop (Fig. 3) can be attributed to capillary condensation effects and variations in pore connectivity. These irregularities are commonly observed in biochar-based materials functionalized with metal oxides, where structural heterogeneities and pore network effects influence nitrogen release during desorption. The presence of NiO and CoO nanoparticles modifies the pore connectivity, causing slight variations in adsorption–desorption equilibrium, which contributes to the observed hysteresis behavior.

The adsorption efficiency of Zn(II) and Cd(II) is strongly influenced by the mesoporous structure of the material. The mesopores in the NiO/CoO@biochar composite (average diameter: 3.31 nm) are comparable to the hydrated radii of

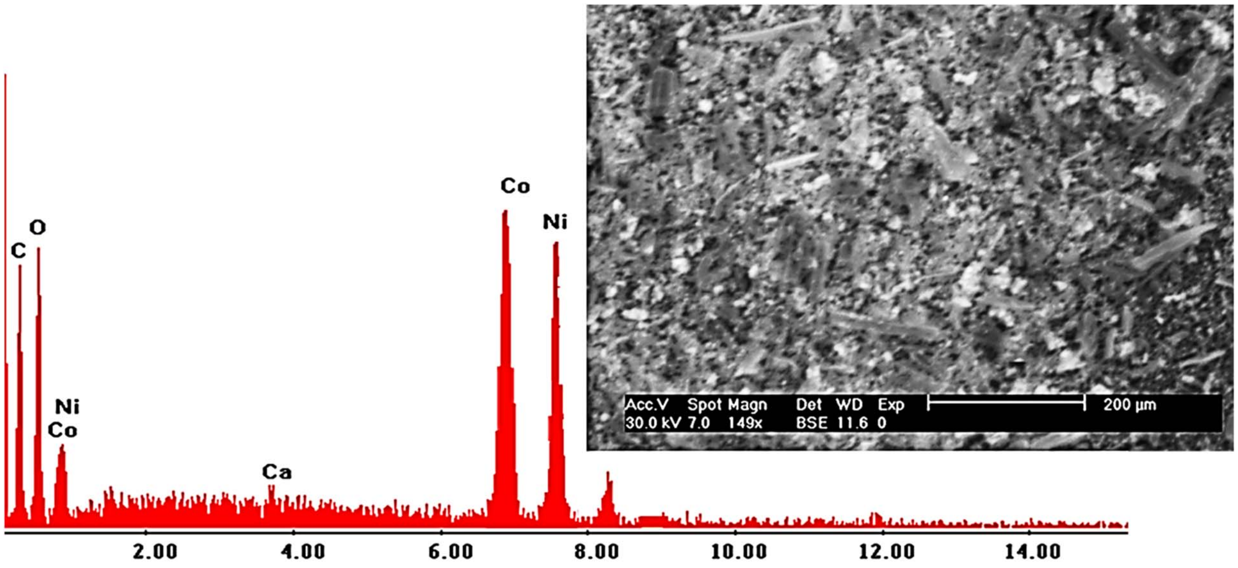

Fig. 4 SEM and EDX spectra of CoO/NiO@biochar.

Table 1 Surface properties of the blank bio-char, and CoO/NiO@bio-char sorbents

Sample name	S_{BET} (m^2 g^{-1})	V_P (cm^3 g^{-1})	D_H (nm)
Blank bio-char	883.29	0.6487	2.9375
CoO/NiO@bio-char	232.55	0.1922	3.3062

Zn(II) (~4.30 Å) and Cd(II) (~4.26 Å),[35] facilitating effective diffusion of metal ions into the porous network and ensuring strong adsorption interactions. If the micropore size were significantly smaller, steric hindrance would limit ion accessibility, reducing adsorption efficiency. Conversely, excessively large pores could lead to weaker binding interactions, lowering selectivity for target metal ions. This study has already established that the NiO/CoO@biochar composite possesses a mesoporous structure with an average pore diameter of 3.31 nm, as determined from BET analysis. Given that mesoporosity is the dominant characteristic, the micropore and mesopore volume differentiation was not explicitly calculated. Instead, the total pore volume measured at $P/P_0 = 0.99$ provides a reliable estimate of the material's porosity, which is sufficient for understanding its adsorption behavior. The adsorption efficiency of Zn(II) and Cd(II) is strongly influenced by the mesoporous structure, as the hydrated ionic radii (Zn(II) ~4.30 Å, Cd(II) ~4.26 Å) are comparable to the composite's mesopore size. This ensures effective diffusion of metal ions without significant steric hindrance. Moreover, the adsorption mechanism involves both electrostatic attraction and surface complexation, further confirming that steric limitations are not a major factor. Therefore, focus of this study was on ensuring a balance between mesoporous structure and functionalized active sites for adsorption rather than explicitly determining micropore and mesopore sizes separately. The incorporation of metal oxides altered the biochar's structure, enhancing ion accessibility while maintaining an optimal pore environment for adsorption. Thus, it can be concluded that the optimized mesoporous structure of the composite plays a crucial role in governing adsorption kinetics and capacity.

Although blank biochar exhibits a high surface area, large pore volume, and a strongly negative surface charge, its adsorption capacity for Zn(II) and Cd(II) is limited by the relatively low density of specific active sites required for strong chemical interactions with metal ions. In contrast, the fabrication of the composite by incorporating NiO and CoO nanoparticles onto the biochar introduces additional reactive sites—such as surface hydroxyl groups—that can form strong inner-sphere complexes with heavy metal ions. These metal oxide sites not only enhance the chemical affinity for Zn(II) and Cd(II) but also create a synergistic effect where the inherent porosity of the biochar facilitates the rapid diffusion of ions to these active sites. Consequently, even though the composite displays a reduction in overall surface area and pore volume compared to the bare biochar, the enhanced chemical functionality and specific binding sites result in a markedly improved adsorption capacity. This approach has been demonstrated in previous studies, which reported that metal oxide-modified biochars significantly outperform unmodified biochar in heavy metal removal.[33] Adsorption of metals in oil sands process water by a biochar/iron oxide composite: influence of the composite structure and surface functional groups.

A detailed pore size distribution (PSD) analysis revealed distinct differences between the two materials. The blank biochar exhibited a unimodal distribution, emphasizing a uniform pore structure, while the NiO/CoO composite showed a bi-modal profile (Fig. 5). This mixed pore system, characterized by both mesopores and micropores, is particularly advantageous for adsorption as it accommodates a range of ion sizes and provides diverse pathways for diffusion. The composite's bi-modal nature reflects the synergistic integration of metal

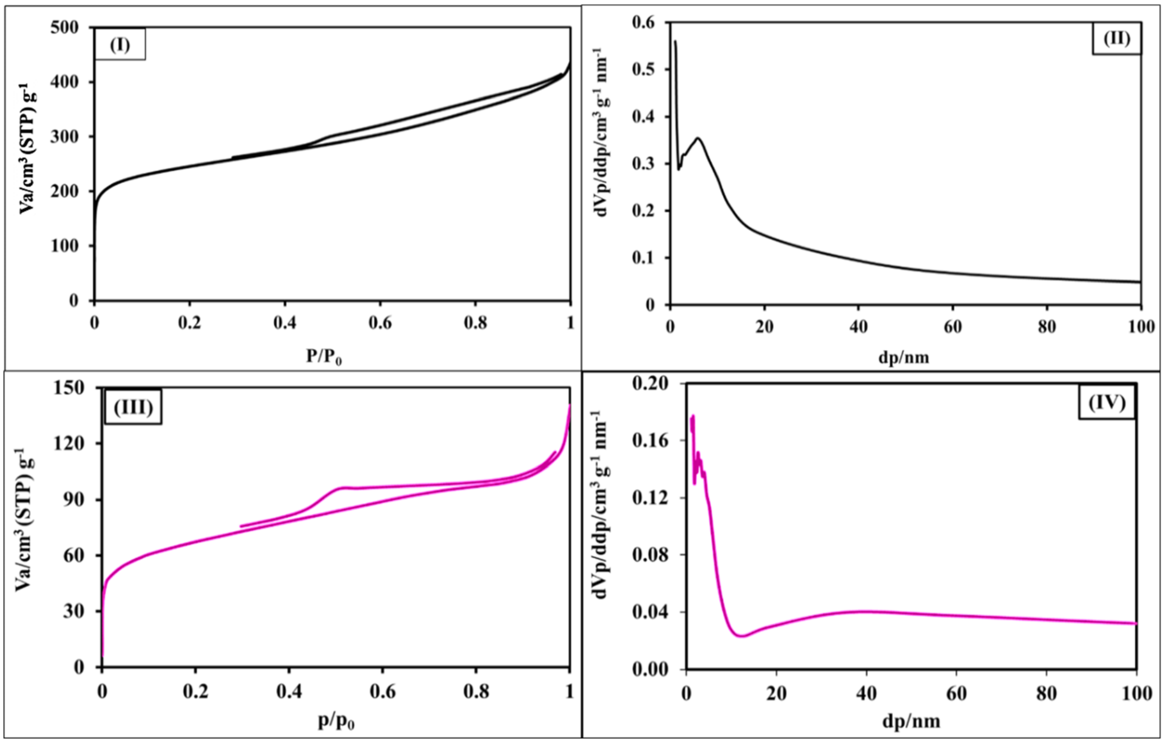

Fig. 5 Isotherms and PSD curves of blank bio-char (I and II) and CoO/NiO@bio-char (III and IV).

oxides into the biochar framework, enhancing its structural complexity and adsorption potential (Fig. 5). The total pore volume of the NiO/CoO composite was found to be 0.1922 cm^3 g^{-1}, compared to 0.6487 cm^3 g^{-1} for the blank biochar, aligning with the observed reduction in surface area (Table 1). The volume of micropores and mesopores was not explicitly calculated, as the dominant mesoporosity of the composite is well-characterized by its BET surface area and BJH pore size distribution. However, the total pore volume measured at $P/P_0 = 0.99$ provides a reliable estimate of the overall porosity, which effectively reflects the material's adsorption potential. More detailed micropore-mesopore volume differentiation, such as NLDFT modeling, could provide additional insights, but given the composite's structural characteristics, such calculations were not deemed essential for this study. The observed differences in surface and pore characteristics underscore the influence of metal oxide loading on biochar's textural properties. These modifications not only alter the physical structure but also enhance the material's functional capabilities, making the NiO/CoO composite a highly effective adsorbent for heavy metal removal.

3.1.6. Particle size & zeta potential analysis. Dynamic light scattering (DLS) analysis revealed that the NiO/CoO@biochar composite exhibited a narrower particle size distribution (250 nm–1.1 μm) compared to the blank biochar (950 nm–2.25 μm) (Fig. 6). Such reduction is referred to the incorporation of metals oxides particles having uniform crystalline shapes, compared to amorphous particles of biochar. Therefore, the reduction in particle size range indicates a more uniform structure, as the narrower distribution suggests a more homogeneous dispersion of particles, which enhances the accessibility of active sites.[23,24]

The average particle size of 830 nm for the composite reflects the successful integration of metal oxides particles which obviously have smaller sizes than those of biochar into its matrix. Hence, such addition of metal oxides of smaller particles in size to biochar structure promotes better dispersion and homogeneity, which is advantageous for adsorption applications (Table 2). Zeta potential measurements provided insights into the surface charge and stability of the materials. The NiO/CoO@biochar composite exhibited a zeta potential of −13.1 mV, while the blank biochar showed a slightly more negative value of −16.7 mV (Table 2). These values indicate moderate colloidal stability, sufficient to prevent aggregation during adsorption processes.[23,24] The incorporation of nickel and cobalt oxides altered the surface chemistry of the composite, slightly reducing its negative charge but improving its capacity to interact with positively charged metal ions such as Zn(ɪɪ) and Cd(ɪɪ).

These characteristics—a narrower particle size distribution and a stable, moderately negative surface charge—enhance the composite's dispersion in aqueous solutions and its ability to capture heavy metal ions. The findings underscore the role of surface charge in facilitating electrostatic interactions, further contributing to the composite's high adsorption efficiency and stability in practical applications.

3.2. Sorption properties

3.2.1. Impact of solution pH and sorbent dose. The solution pH and sorbent dose are pivotal parameters influencing the

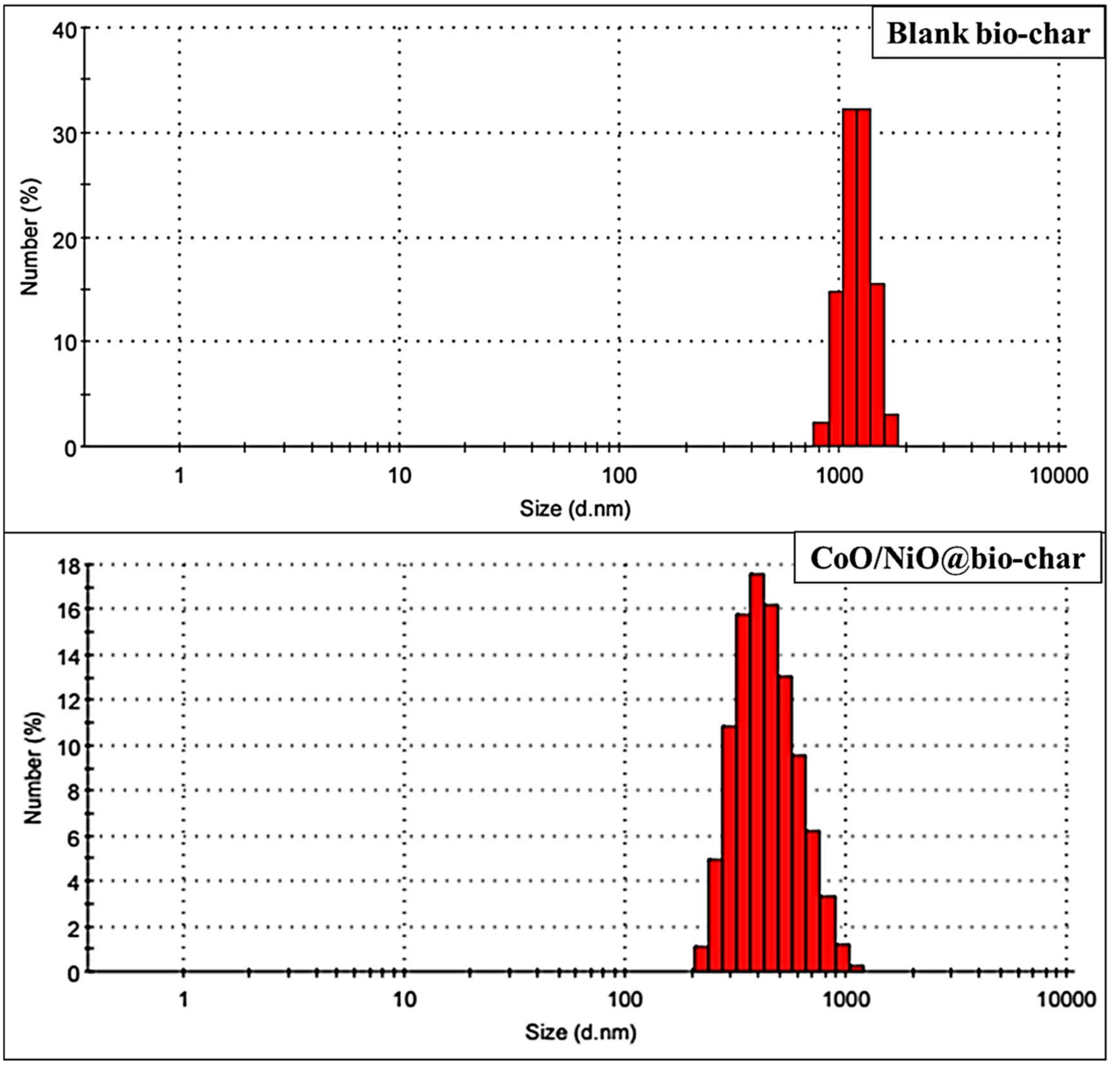

Fig. 6 Particle size distribution of blank bio-char (I), and CoO/NiO@bio-char (II).

Table 2 Surface charges and average particle sizes of bio-char and NiO/CoO@bio-char

Sorbent name	DLS analysis, nm	Zeta potential, mV
Blank biochar	1900	−16.7
NiO/CoO@biochar	830	−13.1

adsorption performance of CoO/NiO@bio-char for Zn(II) and Cd(II) ions. These factors directly affect the adsorbate speciation, surface charge of the sorbent, and availability of active sites, thereby dictating the adsorption efficiency and mechanism.

The effect of pH on Zn(II) and Cd(II) adsorption was studied within the range of 2.0–8.0 at a fixed sorbent dose (3.0 g L^{-1}), shaking time (240 min), initial concentration (40 mg L^{-1}), and room temperature. As shown in Fig. 7(I), the sorption capacity increased with pH, reaching maximum values at pH 6.0 (10.7 mg g^{-1} for Zn(II) and 8.5 mg g^{-1} for Cd(II)). Beyond pH 6.0, the adsorption capacity declined due to the formation of insoluble metal hydroxide species such as ZnO and $Cd(OH)_2$, which reduce the availability of free metal ions for adsorption. The speciation of Zn(II) and Cd(II) in solution at varying pH levels (Fig. S1†) and the zeta potential data for the sorbent (Table 2) help explain the observed adsorption trends.

At low pH values, the high concentration of hydrogen ions (H^+) competes with Zn(II) and Cd(II) for active adsorption sites, leading to suppressed adsorption efficiency.[8–10] As the pH increases, the hydrogen ion concentration decreases, allowing for stronger electrostatic interactions between the negatively charged sorbent (−13.1 mV zeta potential) and cationic species (Zn^{2+}, $ZnOH^+$, and Cd^{2+}). The measured negative zeta potential (Table 2) confirms that the NiO/CoO@biochar composite maintains a negatively charged surface, enhancing metal ion attraction in the optimal pH 4–6 range.

To assess potential ion exchange effects, the equilibrium pH values were recorded post-adsorption, revealing a slight pH increase from 6.00 to about 6.03 for both metal ions. These

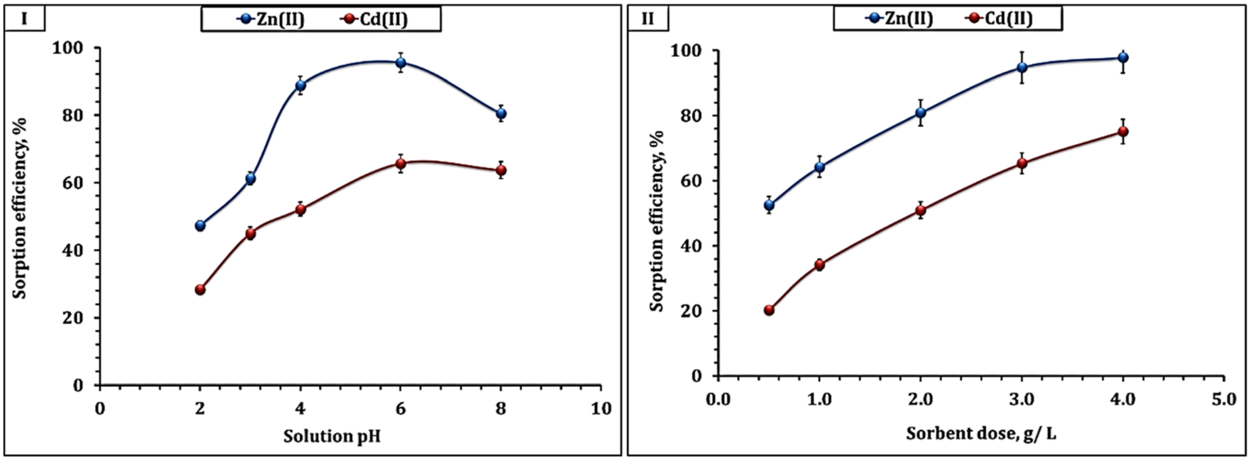

Fig. 7 Sorption efficiency of Zn(II), and Cd(II) depending on (I) function of solution pH (mixing time: 240 min; room temperature; initial concentration: 40 mg L^{-1}; and sorbent dose: 3.0 g L^{-1}), and (II) sorbent dose (room temperature; initial concentration of 40 mg L^{-1}; shaking time of 240 min; solution pH 5.9).

minor pH shifts suggest that adsorption was the dominant removal mechanism rather than precipitation, ensuring that metal uptake primarily occurred *via* electrostatic attraction and surface complexation. However, at pH > 6.0, the predominant presence of insoluble metal hydroxides (ZnO and $Cd(OH)_2$) reduces adsorption affinity, a trend consistent with the surface complexation formation (SCF) theory.[36,37] Similar findings have been reported by Gupta *et al.*,[2] El-Said *et al.*,[3] and others,[7–10] supporting the conclusion that electrostatic interactions and surface complexation are the primary adsorption mechanisms within the optimal pH range (4–6). The stable equilibrium pH values further confirm that metal precipitation effects were minimal, ensuring that adsorption, rather than chemical precipitation, governed metal removal efficiency.

In respect to the impact of sorbent dose on adsorption process, a set of experiments were evaluated over a range of 0.5–4.0 g L^{-1}. As illustrated in Fig. 7(II), the adsorption percentage of Zn(II) and Cd(II) increased with higher sorbent doses, attributed to the greater surface area and availability of active sites.[8–10] However, the adsorption capacity (qe_{exp}) decreased significantly from 41.9 to 9.8 mg g^{-1} for Zn(II) and from 16.2 to 7.5 mg g^{-1} for Cd(II) as the sorbent dose increased. The slight decrease in adsorption capacity at higher sorbent dosages can be attributed to the adsorbent-dose effect, where the excess of available active sites relative to metal ion concentration leads to underutilization of the sorbent's adsorption potential. Additionally, at higher doses, particle aggregation may reduce effective surface area, limiting accessibility to adsorption sites.[2,3] The selected 3.0 g L^{-1} dose balances high removal efficiency and accurate kinetic modeling, ensuring adsorption equilibrium is achieved within a measurable timeframe. Furthermore, distribution coefficient (K_d) values, calculated from experimental data, showed significant variations with changing sorbent doses (Fig. S2†). This indicates the strong complexation of Zn(II) and Cd(II) ions with the functional groups on the CoO/NiO@bio-char surface.[38–40] These results highlight the critical role of optimizing both solution pH and sorbent dose to maximize adsorption performance. Understanding the interplay of these parameters provides valuable insights into designing efficient sorption systems for heavy metal removal.[38]

3.2.2. Uptake kinetics. The adsorption kinetics of Zn(II) and Cd(II) ions using CoO/NiO@bio-char were studied to elucidate the adsorption mechanism and determine the rate-controlling steps. Experiments were conducted by monitoring adsorption capacity (qtq_tqt) over time, ranging from 5 to 600 minutes, at a solution pH of 5.9, room temperature, an initial metal ion concentration of 40 mg L^{-1}, and a sorbent dose of 3.0 g L^{-1}. The kinetic curve (Fig. 8(I) and (II)) illuminates that both metal ions showed a similar kinetic profile but with different magnitudes. Initially, there was a rapid increase in the adsorption capacity (fast rate of reaction) for both metal ions, which continued up to 60, and 120 minutes (equilibrium point) for Zn(II), and Cd(II) respectively. After this point, the adsorption capacity almost remained constant (flat shape). This behavior can be explained by the presence of free sorbent active sites at the beginning of the adsorption process, which enhances the interaction between the sorbent and the metal ions and improves the rate of reaction. Additionally, the concentration gradient generated by the mass transfer driving forces overcomes the external resistance and facilitates the diffusion of the metal ions to the sorbent surface, thus increasing the rate of reaction.[37,38] As the equilibrium time is extended, most of the surface function groups become bound to the metal ions, and the intra-diffusion mechanism takes place, resulting in a slight variation in the kinetic curve (plateau shape) where the rate of the adsorption process is equal to the rate of the desorption process.[37,38]

The results of an experiment were analyzed using different kinetic models, namely the Pseudo-first-order, pseudo-second-order, and Weber and Morris (intraparticle diffusion) models, to understand the adsorption process better.[25–28] The terms of the models are shown in Table 3. The data gathered showed that the pseudo-first-order and pseudo-second-order models had a strong correlation coefficient ($R^2 \geq 0.95$) for both metal ions. However, the pseudo-second-order model had the lowest

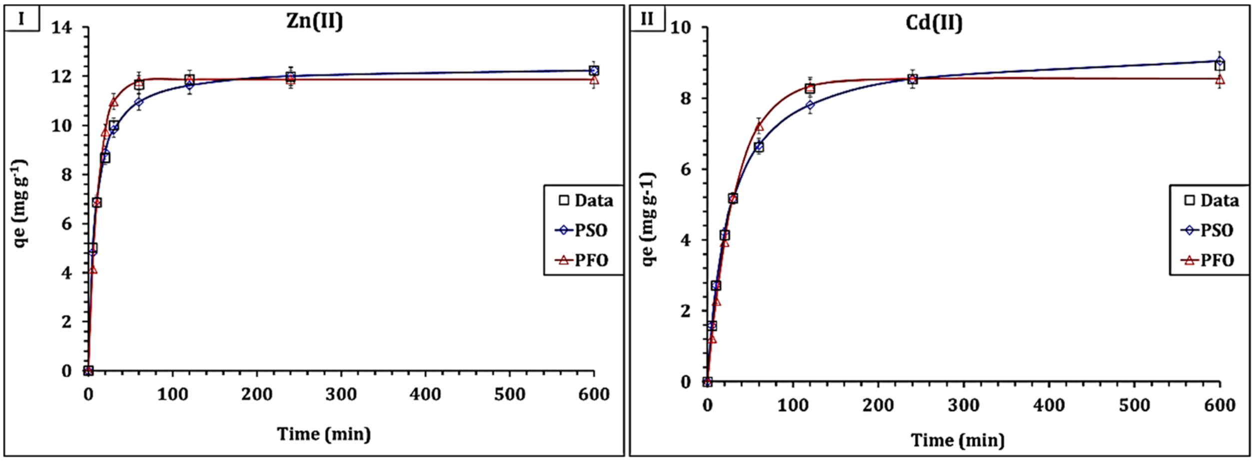

Fig. 8 (I) The kinetic curve of Zn(II) and (II) Cd(II) uptake process (solution pH 5.9; temperature of 25 ± 1 °C; initial concentration of 40 mg L^{-1}; sorbent dosage of 3.0 g L^{-1}).

average relative error (ARE = 2.1, and 1.3 for Zn(II) and Cd(II) respectively), indicating that it fits better for the adsorption process. This suggests that the uptake of Zn(II) and Cd(II) is a chemisorption process and that an electron sharing or transfer process occurs during the interaction between both metal ions and the CoO/NiO@bio-char sorbent.[25–28] Notably, the calculated adsorption capacity equals 15.5, and 11.7 mg g^{-1} for Zn(II), and Cd(II) respectively, and the rate constant for Zn(II) and Cd(II) is 0.009 and 0.003 $\min^{-1}$ respectively, which reflects a higher affinity for Zn(II) ions than Cd(II) ions. In addition, the initial sorption rate (h = 2.1 and 0.5 mol g^{-1} h^{-1} for Zn(II) and Cd(II) respectively), and the half-equilibrium time ($t^{0.5}$ = 7.4 and 24.8 h for Zn(II) and Cd(II) respectively) reveal that Zn(II) adsorption process exhibit a faster rate of reaction than Cd(II) adsorption process which is consistent with the experimental findings.

The same kinetic attitude (chemisorption process) was depicted for Zn(II), and Cd(II) removal from aqueous solution using other sorbents such as Wood ash amended biochar,[1] potato starch phosphate (PSP) polymer,[2] Rice husk ash (RHA),[3,18] cross-linked reusable polystyrene adsorbents (PS-NH-DCDEE, and PS-NH-TCE),[7] bentonite/polypyrrole (B-Ppy) composite,[12] and Thermal power plant fly Ash.[38]

Weber–Morris model is used for analyzing the experimental results to explore the diffusion mechanism of Zn(II), and Cd(II) ions using CoO/NiO@bio-char.[25–28] The model terms were evaluated from the plot of sorption capacity (q_t) against $\text{time}^{0.5}$ (Fig. S3†) and displayed in Table S2.† As can be seen, both metal ions exhibit a multi-linear relationship, which deduced that the adsorption process is controlled by multiple mechanisms (*i.e.* chemical and physical mechanisms).[16–18] Initially, the adsorption process is characterized by the presence of many free surface active sites and a high ion concentration, resulting in low boundary resistance and a high rate of reaction, which means a fast process.[16–18] So far, chemical reaction mechanisms such as complexation mechanisms are involved during this stage. Beyond reaction equilibrium, the boundary layer resistance is increased, and most of the surface active sites are occupied with the ions therefore, the metal ions diffuse inside the pores of the sorbent, leading to a sluggish adsorption process.[16,18] Physical adsorption mechanisms, such as the intra-particle diffusion mechanism, take place at this stage.[16,18]

Table 3 The values of the applied kinetics model parameters

	Zn(II)	Cd(II)
Pseudo first-order model		
q_1 (mg g^{-1})	14.8	10.7
k_1 ($\min^{-1}$)	0.1	0.03
ARE	5.6	7.07
R^2	0.95	0.99
Pseudo second-order model		
q_2 (mg g^{-1})	15.5	11.7
k_2 ($\min^{-1}$)	0.009	0.003
h (mol g^{-1} h^{-1})	2.1	0.5
$t_{1/2}$ (h)	7.4	24.8
ARE	2.1	1.30
R^2	0.99	0.99

3.2.3. Sorption isotherms – equilibrium performance. The graphs in Fig. 9 show the sorption isotherm of Zn(II) and Cd(II) ions using CoO/NiO@bio-char. It represents the relationship between the sorption capacity (q_e) and the residual concentration (Ce) of the metal ions. The asymptotic shape of the sorption isotherm shows a preference for metal ions according to the series: Zn(II) > Cd(II), nevertheless, the sorption performance of both metals is the same whereas the figure has two distinct parts. The first part, which extends up to 10 mg g^{-1} for both metal ions, is depicted by a steep initial section that indicates the high affinity of the resins for Zn(II) and Cd(II) ions. This is presumably due to the active functional groups on the CoO/NiO@bio-char surface that bind to metal ions.[35,40] In the second part, the curves tend to reach a plateau, with a slight increase in the sorption capacity, for residual concentrations >10 mg L^{-1}. This is because almost all the functional groups on the sorbent surface have become saturated.[35,40,41]

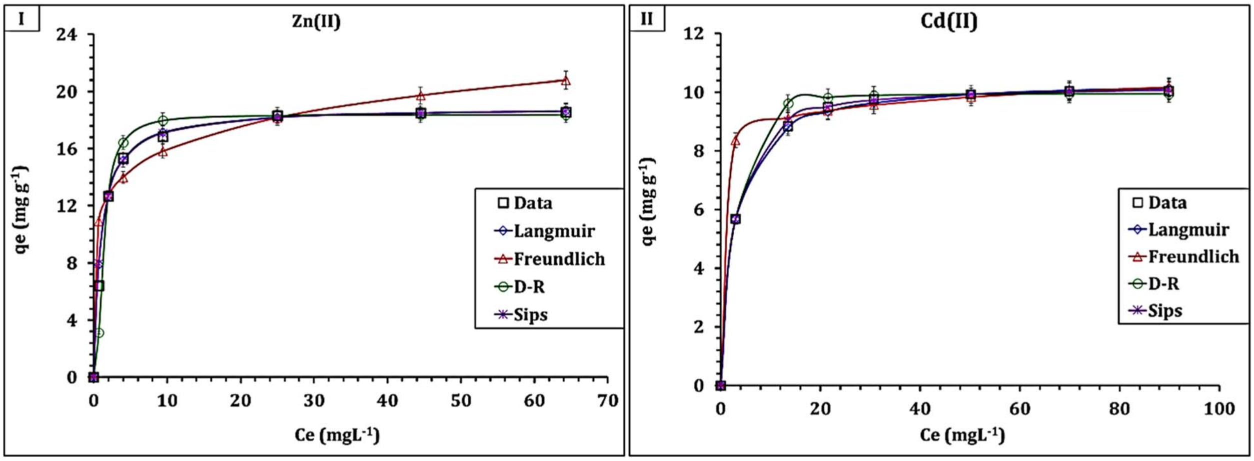

Fig. 9 (I) Isotherm profile for the adsorption of Zn(II) and (II) Cd(II) ions from aqueous using CoO/NiO@bio-char (temperature of 25 ± 1 °C; pH 5.9; sorbent dosage of 3.0 g L^{-1}; shaking time is 240 min).

The uptake isotherm is profoundly dissected by analyzing the experimental results using the following isotherm models; Langmuir, Freundlich, D–R, and Sips models.[27–30] The terms of the isotherm models were evaluated and displayed in Table 4. The displayed data shows that the Zn(II) and Cd(II) ions sorption process obeys the Langmuir model whereas it exhibits the lowest (ARE) values (3.7, and 1.1) and the highest (R^2) values (0.99) for both Zn(II) and Cd(II) ions respectively. This indicates that the removal is a monolayer process, and CoO/NiO@bio-char has a uniform and homogenous surface, which is consistent with the SEM analysis (Fig. 4). Similar isotherm behavior (*i.e.* monolayer, and homogeneous process) was elucidated for Zn(II), and Cd(II) adsorption from aqueous solution using other sorbents such as Wood ash amended biochar,[1] potato starch phosphate (PSP) polymer [2], Rice husk ash (RHA),[3,18] cross-linked reusable polystyrene adsorbents (PS–NH-DCDEE, and PS-NH-TCE),[10] bentonite/polypyrrole (B-Ppy) composite,[12] and Thermal power plant fly Ash.[37]

The sorption isotherm provides two important insights: (I) the maximum sorption capacity achieved at the sorbent saturation, and (II) the sorbent affinity for the metal ions.[35,40] The data in Table 4 shows that The sorption capacities at saturation of monolayer (*i.e.*, q_m) are 18.9 and 10.2 mg g^{-1} for Zn(II) and Cd(II) respectively, which is roughly consistent with the experimental values of maximum sorption capacities (18.6 mg/g for Zn(II), and 10.0 mg/g for Cd(II)). The affinity coefficient (*i.e.*, k_L) for Zn(II) is higher than that for Cd(II) which confirms the higher tendency of the applied sorbent towards Zn(II) than Cd(II). The same behavior (higher affinity to Zn(II) ions than Cd(II) ions) was recognized by other sorbents such as Wood ash amended biochar,[1] potato starch phosphate (PSP) polymer,[2] Rice husk ash (RHA),[3,18] cross-linked reusable polystyrene adsorbents (PS-NH-DCDEE, and PS-NH-TCE),[10] bentonite/polypyrrole (B-Ppy) composite,[12] and Thermal power plant fly Ash[37] during the adsorption of heavy metal ions from aqueous solution.

Table 4 The values of the applied isotherm model parameters

	Zn(II)	Cd(II)		Zn(II)	Cd(II)
Langmuir model			**Freundlich model**		
q_m (mg g^{-1})	18.9	10.2	$1/n_F$	0.1	0.1
k_L (L mg^{-1})	1.0	0.7	k_F (mg g^{-1}) (mg L^{-1})	11.5	7.9
ARE	3.72	1.11	ARE	14.89	7.19
R^2	0.99	0.96	R^2	0.79	0.76
D–R model			**Sips model**		
q_D (mg g^{-1})	18.4	10.0	q_S (mg g^{-1})	18.9	10.2
B (mol^2 kJ^{-2})	0.4	0.5	k_S (L mg^{-1})	1.0	0.7
E_{ad}	1.2	0.99	m_S	1.0	1.0
ARE	9.5	1.98	ARE	3.93	1.12
R^2	0.97	0.99	R^2	0.99	0.99

Many factors, including hydration ion radii, ion hydrolysis constants, metal ion electronegativity, and hydration energy, have a significant impact on the sorbents' affinity for ions.[35,42,43] The effect of ionic radii and the hydration energy (ΔH_{hyd}) on the Zn^{2+}, Cd^{2+}, and Pb^{2+} selectivity of EDTA-modified maize cob was also mentioned by Igwe and Abia.[44] According to Mihajlović *et al.*[45] the hydrated cation radii, hydration energy, and electronegativity of the ions were shown to be correlated with the affinity of natural and modified zeolite towards various metals, with $Pb^{2+} > Cd^{2+} > Zn^{2+}$ being the most preferred. According to Page *et al.*,[46] the cation hydration energy has an impact on the REE's strength over Al and Fe(III) adsorption onto a sulfonic acid resin.

In this study, hydrated zinc and cadmium metal ions were compared in terms of their ion radius ($CdH_2O_6^{2+}$ (0.96 Å); and $ZnH_2O_6^{2+}$ (0.74 Å)) and hydration energy (Zn(II) (−2046 kJ Mol^{-1}), and Cd(II) (−1807 kJ Mol^{-1})).[35,47,48] It was observed that the sorption affinity is inversely proportional to the ion radius, meaning smaller ions are easier to penetrate an adsorbent. This observation has also been reported previously by Salam *et al.*[10] Based on hydration energy, Zn(II) is expected to have a greater sorption strength than Cd(II). This matches the obtained data in the study, which shows that the sorption capacity is positively impacted by an increase in metal ions' hydration energy. The same observation has been reported by Igwe and Augustine.[44]

The electronegativity values of zinc and cadmium, ions are reported as 1.55 and 1.90 respectively. So the biochar affinity towards the capture of both Zn and Cd ions could be non-correlated to this parameter where it has no critical influence on its tendency to sorption of these metal ions. The hydrolysis constant (pK_a) of the metal ions could be sequenced as Cd(II) 10.01 > Zn(II) 9.15. This means that the affinity of CoO/NiO@bio-char is almost affected positively with the decrease of the metal ion hydrolysis constant. This may be due to that the lower the hydrolysis constant of an ion, the higher its tendency to form hydrolysis products, and in turn more competition toward charged sorbent surfaces.[10] This behavior disagrees with Nayak *et al.*,[16] and Mihajlović *et al.*[45] According to the Pearson Hard/Soft Acids and Bases (HSAB) theory, metal ions are classified based on their behavior as electron acceptors (acids) or electron donors (bases).[35,42] This classification helps interpret the strength of metal binding. Strong acids preferentially react with strong bases, while weak acids react with weak bases.[49] Zinc is considered a borderline acid, and cadmium is considered a soft acid based on the HSAB theory, with their Lewis acid strengths being 0.405 and 0.32, respectively.[35,42] This means that the function group of the CoO/NiO@bio-char will have a higher affinity for zinc than for cadmium ions. The experimental results obtained in this study are in harmony with the HSAB theory, indicating that zinc ions exhibit stronger binding than cadmium ions.

It is noteworthy that the adsorption isotherm of Zn(II), and Cd(II) ions onto the blank bio-char obeyed to Langmuir isotherm model (Table S3†), which illuminated that both blank bio-char and CoO/NiO@bio-char exhibits similar isotherm behavior (*i.e.* monolayer, and homogeneous process). The comparison between the affinity of both carbonaceous species to Zn(II), and Cd(II) ions declares that The adsorption capacity of the composite was significantly higher than that of biochar alone, with maximum capacities of 18.9 mg g^{-1} for Zn(II) and 10.2 mg g^{-1} for Cd(II), compared to 7.0 mg g^{-1} and 8.5 mg g^{-1} for biochar, respectively. Although biochar has a higher surface area and pore volume (Table 1), the composite exhibits higher adsorption capacity due to the presence of metal oxides, which provide additional active sites for adsorption. The metal oxides also enhance the electrostatic interactions between the adsorbent and the metal ions, leading to improved adsorption performance. This illuminates that the activation process improves the texture properties of the blank bio-char. This is consistent with the insights from the sorbent characterization results (Section 3.1). Nevertheless, blank biochar sorbent exhibits a higher affinity to cadmium ions than zinc ions. This performance could be attributed to strong dependency on its function groups (acting as bases), during the adsorption process, to attract the species of Cd ions which have stronger acidic strength than Zn ions.

It is possible to examine the sorption process profile by using the dimensionless equilibrium parameter R_L, which is equal to $1/(1 + K_LC_o)$.[27–30] The sorption can be categorized as irreversible ($R_L = 0$), linear ($R_L = 1$), unfavorable ($R_L > 1$), or favorable ($0 < R_L < 1$).[27–30] The values of R_L were assessed and are presented in Fig. S4.† The data demonstrates a favorable sorption process where R_L values vary between 0.01 to 0.03 for Zn(II), and from 0.02 to 0.06 for Cd(II) for all initial concentrations that were investigated.

The Sips equation, which is based on the Langmuir–Freundlich concept, includes a third adjustable parameter that is meant to enhance the accuracy of curve fitting.[27–30] This is supported by the lower ARE and higher R^2 values obtained. The calculated sorption capacity for Zn(II) and Cd(II) (18.9 and 10.2 mg g^{-1}) aligns with the calculated sorption capacity from the Langmuir model. The Freundlich model represents multilayer adsorption on heterogamous surfaces.[27–30] It has the lowest coordination coefficient and the highest ARE coefficient. However, it fits well at a low initial concentration as shown in Fig. 9. The term ($1/n$) can be used to determine the adsorption intensity of a substance. A sorption process is considered favorable if the value of $1/n$ is less than one but greater than zero. If $1/n$ equals one, the process is irreversible. If $1/n$ is greater than one, then the process is unfavorable.[27–30] Table 4 indicates favorable sorption for Zn(II) and Cd(II) with $1/n$ values of 0.1. The same conclusion was reached using the Langmuir dimensionless parameter R_L.

The Dubinin–Radushkevich model, which follows the pore-filling mechanism, suggests that a multilayer adsorption process through van der Waals's forces could occur during the Zn(II) and Cd(II) ions adsorption process.[27–30] This is supported by proper coordination and ARE coefficient values. The maximum sorption capacity (q_{ad}) was found to be 18.4 and 10.0 mg g^{-1} for Zn(II) and Cd(II) respectively, which is close to the maximum sorption capacity calculated from the Langmuir model. The mean free energy (E_{ad}, kJ mol^{-1}) can be used to determine the nature of the sorption process. $E < 8$ kJ mol^{-1} reflects a physisorption process, whereas $8 < E < 16$ kJ mol^{-1} indicates a chemisorption process.[27–30] In this case, the data in Table 4 suggests a physisorption process since $E \leq 1.2$ kJ mol^{-1}. Finally, isotherm investigation confirms that both metal ions' sorption process is controlled by multiple reaction mechanisms, which is consistent with the achievement of the Webber-Morris kinetic model.

To further evaluate the adsorption performance of the NiO/CoO@biochar composite, a comparative analysis with previously reported adsorbents was conducted and is summarized in Table 5. This table presents a direct comparison of adsorption capacities under various experimental conditions, including metal ion concentration, pH, contact time, and temperature, providing a meaningful assessment of our composite's efficiency. The results demonstrate that the NiO/CoO@biochar composite exhibits a competitive or superior adsorption capacity compared to other biochar-based and metal-oxide-modified adsorbents. This enhancement can be attributed to the synergistic effect of metal oxide incorporation, which increases surface functional groups, enhances electrostatic interactions, and improves adsorption affinity toward Zn(II) and Cd(II) ions. Unlike a direct correlation between BET surface area and adsorption capacity, which may not fully account for adsorption efficiency, the combination of textural properties and surface chemistry plays a critical role in metal ion uptake. Thus, the comparative analysis in Table 5 effectively

Table 5 Comparison of sorption performance of Zn(II), and Cd(II) for different sorbents

Sorbent type	Co, mg L^{-1}	pH	Time, h	q_e, mg g^{-1}	R
Zn(II)					
Rice husk ash (RHA)	10–100	6.0	6	3.5	3
Natural foxtail millet shell	25–300	5.0	2	10.6	6
Wood ash amended biochar	10–150	4.7	48	12.1	8
$KMnO_4$/hematite te modified biochar	5–100	6.0	24	14.2	9
Bentonite/polypyrrole composite	1–20	5.0	1	6.6	17
Rice husk ash	10–100	6.0	5	3.0	18
Durian peel	10–200	8.0	4	36.6	22
Thermal power plant fly ash	1–20	6.0	2	1.4	35
Blank bio-char	20–120	6.0	4	7.0	PW
CoO/NiO@bio-char				18.9	
Cd(II)					
Rice husk ash (RHA)	10–100	6.0	6	2.1	3
Natural foxtail millet shell	25–300	5.0	2	12.5	6
Wood ash amended biochar	10–150	4.7	48	10.2	8
$KMnO_4$/hematite modified biochar	5–100	6.0	24	17.3	9
Bentonite/polypyrrole composite	1–20	5.0	1	3.2	17
Rice husk ash	10–100	6.0	5	5.8	18
Thermal power plant fly ash	1–20	8.0	2	4.7	35
Blank bio-char	20–120	6.0	4	8.5	PW
CoO/NiO@bio-char				10.2	

contextualizes our findings within the literature and highlights the adsorption potential of NiO/CoO@biochar under practical conditions.

3.2.4. Impact of reaction temperature and thermodynamic investigation. The dependence of CoO/NiO@bio-char sorption capacity on the adsorption temperature (Fig. 10(I)) illuminates the thermodynamic performance of the uptake process. As can be seen, both elements exhibit the same performance whereas, the adsorption capacity is positively impacted from 12.4 to 12.9 mg g^{-1} for Zn(II) and from 8.4 to 9.4 mg g^{-1} for Cd(II) with the rose of reaction temperature which reflects an endothermic nature for the uptake process.[31,32] Thermodynamic equations that displayed in (Table S1†) and Van't Hoff plot (Fig. 10(II)) are used to explore the sign and the values of the thermodynamic terms (*i.e.* standard Gibbs free energy change ($\Delta G°$), standard enthalpy change ($\Delta H°$), and standard entropy change ($\Delta S°$)) as declared in Table 6. The anticipated results confirm that the

Table 6 The evaluated thermodynamic parameters

	ΔG (kJ mol^{-1})				ΔH	ΔS
	20 °C	30 °C	40 °C	50 °C	(kJ mol^{-1})	(J mol^{-1} K^{-1})
Zn(II)	−20.9	−21.6	−23.5	−25.0	29.6	169.5
Cd(II)	−15.7	−16.2	−16.9	−17.9	10.0	86.3

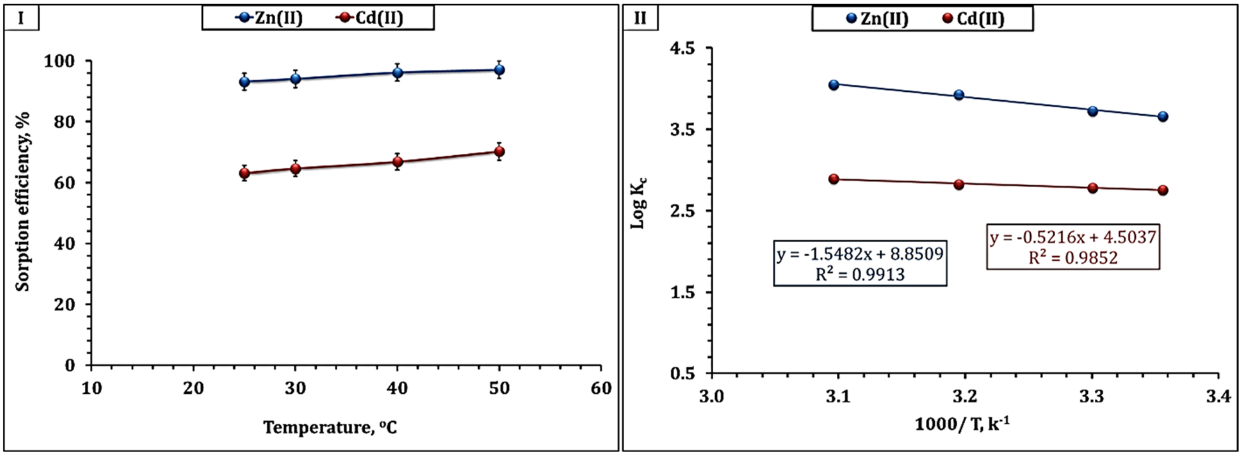

Fig. 10 (I) impact of reaction temperature of Zn(II) and Cd(II) sorption capacity (40 mg L^{-1} initial concentration; sorbent dose of 3.0 g L^{-1}; pH 5.9; shaking time is 120 min), (II) thermodynamic profile for the adsorption process.

adsorption process is endothermic, with a positive Δ*H*° value (29.6 and 10.0 kJ mol^{-1} for Zn(II) and Cd(II) respectively).[31,32] It is noteworthy that the value of Δ*H*° is less than 84 kJ mol^{-1}, which indicates that the sorption process is caused by a physical mechanism (physisorption).[31,32] The same finding is recognized by the analysis of the experimental results using the D–R isotherm model in Section 3.2.4. A spontaneous and feasible adsorption system could be recognized from the negative value of the standard Gibbs free energy change values. It is noteworthy that the negative value of Δ*G*° increased as the reaction temperature increased which reflects the favorability of the adsorption process to the reaction temperature increment.[31,32] The positive standard entropy change value (169.6, and 86.3 J mol^{-1} K^{-1} for Zn(II) and Cd(II) respectively) suggests that there is an increase in randomness at the solid-solution interface during the uptake process which reflects structural changes onto the sorbent surface through the adsorption.[31,32] Bashir *et al.*,[2] Andelescu *et al.*,[50] Golgoli *et al.*[36] and Venkata[38] deduced similar thermodynamic performance (*i.e.* endothermic, spontaneous, and feasible process) for Zn(II), and Cd(II) adsorption

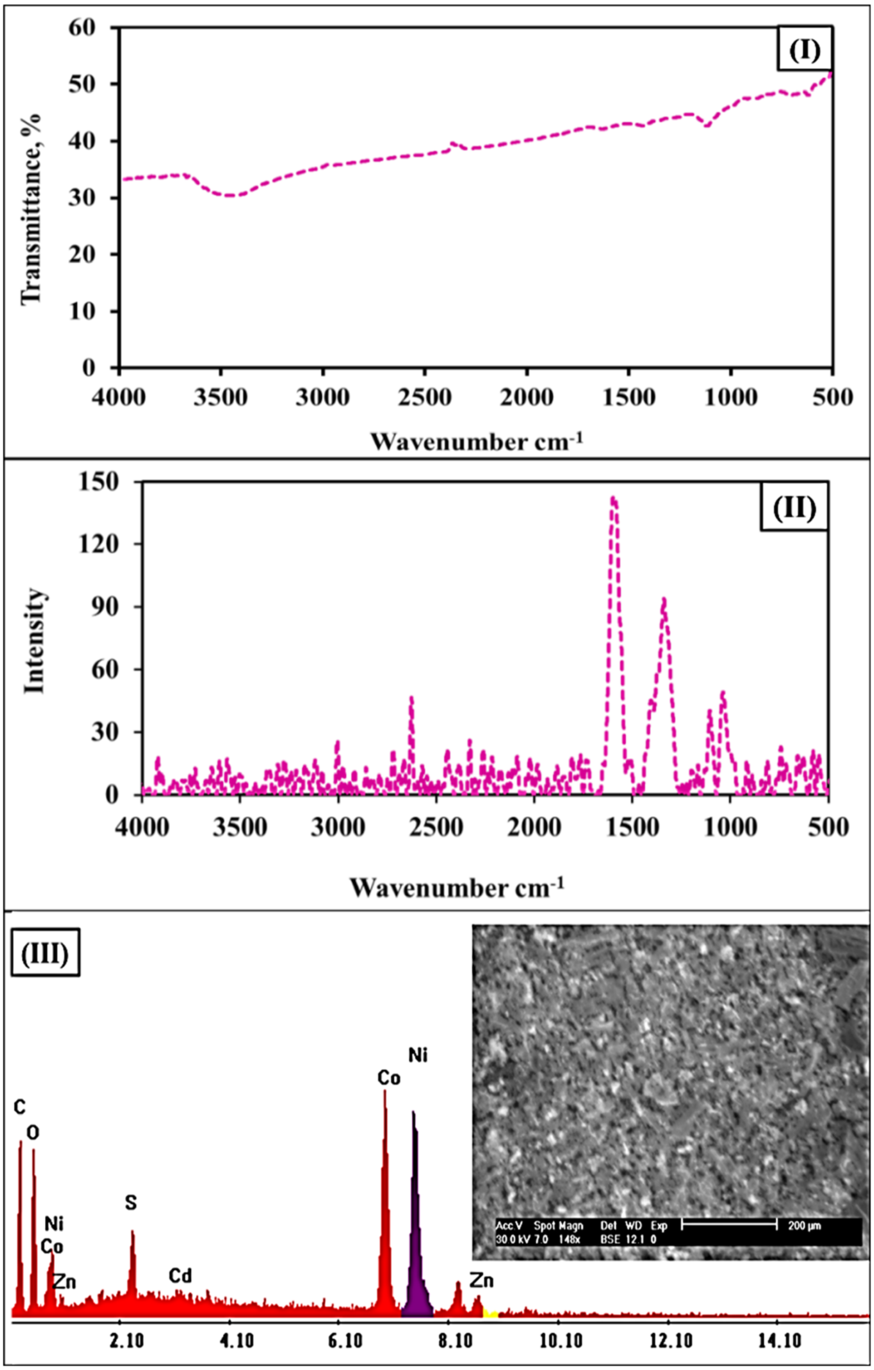

Fig. 11 FTIR (I), Raman (II), and EDX spectra (III) for spent adsorbent.

Table 7 Surface charges and average particle sizes for both bio-char and metal oxide composites before and after the adsorption of Zn/Cd(II) ions

	DLS analysis, nm		Zeta potential, mV	
Sorbent name	Before	After	Before	After
Blank charcoal	1900	3560	−16.7	−6.4
CoNi@charcoal	830	1798	−13.1	−1.9

from aqueous solution using cysteine-functionalized selenium nanoparticles (SeNPs), Thermal power plant fly Ash, potato starch phosphate (PSP) polymer, and magnetite/carbon nanocomposites respectively.

3.2.5. Characteristics of spent adsorbents. Determining the characteristics of the spent adsorbents is an essential stage to further verify their activities toward the removal of designated species. In the current study, features of the spent adsorbent, after being employed in the disposal of zinc and cadmium cations, are illustrated through the provided data in Fig. 11 and Table 7. Observable decreases in zeta potential values of the spent adsorbents were detected, referring to their increased tendency to segregate out of a suspension due to their limited ability to form properly stable dispersed particles. These declines could be explained by the aggregation of zinc/or cadmium ion species onto the particles of the composite structure, leading to its deposition in the processing media.[16,18] The variation of zeta potential was accompanied by massive increases in the average particle sizes of the spent adsorbents which verified their successful carry-up of zinc/or cadmium ions which resulted in enlargement in particle size, compared to the fresh adsorbent. Elimination of such species, from the aqueous solution, was also admitted through the given FTIR spectrum where the intensities of the detected peaks had strongly varied and were quite deformed, in comparison to their corresponding in the freshly-made adsorbent. Further verification for the removal of zinc/cadmium species was done by observing its indicative peaks in the exhibited EDX pattern.

Additionally, Raman spectroscopy of the spent adsorbent (Fig. 11(II)) provides further evidence of chemisorption through noticeable spectral shifts and the emergence of new vibrational bands. Compared to the fresh CoO/NiO@bio-char, the spent adsorbent exhibits additional peaks below 500 cm^{-1}, which correspond to Cd–O and Zn–O bond formations, indicating strong chemical interactions between the metal ions and the adsorbent surface. Moreover, a newly observed peak around 1000 cm^{-1} is attributed to possible metal–metal interactions (Ni–Zn, Co–Zn, Ni–Cd, or Co–Cd) or complexation between biochar functional groups and the adsorbed metal ions. These spectral changes confirm that the adsorption process is not purely physical but involves chemical bonding, reinforcing the findings from FTIR and kinetic modeling that suggest an inner-sphere complexation mechanism. The disappearance or broadening of characteristic D- and G-band features further supports the structural modifications induced by metal ion coordination, highlighting the role of chemisorption in the removal process.

3.2.6. The proposed mechanism. The effectiveness of biochar in absorbing metal ions is influenced by various factors including the chemistry of the metal ion in solution, and the morphology and texture properties of the bio-char.[2,51] The adsorption of metal ions using biochar is a complex process involving several mechanisms, including physical adsorption, electrostatic interaction, ion exchange, precipitation, and complexation.[8–10,16,36,37] Studies have shown that the precipitation of metal ions with minerals contained in biochar is the dominant mechanism for metal ion sorption.[8,9] However, other studies have suggested that the cation exchange mechanism and surface complexation between metal ions and the oxygen-containing functional groups of biochar are also significant factors.[9,10,16,37] Additionally, the cation–π interactions mechanism is involved in metal ions sorption using bio-chars with highly cyclic aromatic structures, and the biochar can be used as a π-donor.[9,51] On the other hand, the electrostatic attraction mechanism is expected for metal ions sorption using biochar with pHpzc < solution pH, where the biochar surface becomes negatively charged and is attracted to positively charged cation species.[9,10,16] The large surface area and proper micropore structure of biochar enhance the contribution of the physical adsorption mechanism for removing metal ions from an aqueous solution.[2,10,16]

In the present study, the zeta potential analysis declares that the synthesized CoO/NiO@bio-char sorbent exhibits a negatively charged surface value, while the speciation of Zn(II) and Cd(II) ions over the different pH values of the aqueous solution (Fig. S1†) displayed a cationic species (mainly, Zn^{2+}, $ZnOH^{+}$, and Cd^{2+}), deducing the occurrence of electrostatic interaction between the negative charge on surfaces of the carbonaceous material and the positive cation species. This proposal is confirmed by the zeta potential analysis of the carbonaceous sorbent after the adsorption process, whereas the charge negativity of the sorbent surfaces decreased from −13.1 to −1.9 mV due to their uptake of positive divalent cations. On another side, the obvious boost in the particle size after the adsorption process confirms the outer-sphere complexes between the sorbent's surfaces and Zn/or Cd ions. Furthermore, the capture of both metal ions could take place *via* inner-sphere complexes with the present hydroxyl function group on the surface of the composite Carbonaceous sorbent. The surface complexation mechanism could be confirmed by the noted variations in FTIR analysis for the CoO/NiO@bio-char before and after the uptake process (Fig. 2, and 11 respectively). Particularly, the indicative peak of the –OH group in FTIR spectra showed obvious changes after the adsorption process (Fig. 11), compared to the corresponding fresh adsorbent (Fig. 2), reflecting the taking part of the complex formation mechanism in the removal process. This mechanism is consistent with the findings of the kinetic analysis results, which revealed that the Pseudo-second order kinetic model is the best fit for describing the adsorption process, which reflects the chemisorption interaction through the inner surface complexation mechanism. Additionally, the newly observed peaks in Raman analysis of the spent adsorbent could further confirm chemisorption occurrence as well as the presence of metal–metal interaction between the sorbent particles and contaminating metal cations. On the other side, adsorption through the diffusion of Zn and Cd ions within the sorbent pores (pores trapped mechanism) is also present owing to the smaller radii of these ions than average pores radii of the adsorbent, as presented in Table 1 (surface characteristics).

The morphology and texture investigation of the CoO/NiO@bio-char sorbent explores that it has a uniform and porous surface. This indicates that physical sorption mechanisms could play a role, in addition to chemisorption mechanisms, particularly prolong the equilibrium state. This finding is consistent with the insights from the W-M kinetic model which explores that the intraparticle diffusion of the metal ions over the sorbent pores contributes to the adsorption process by extending the equilibrium time. SEM (Fig. 11) analysis of the spent CoO/NiO@bio-char confirmed this finding, as many of the crevices on the sorbent surface disappeared (Fig. 3). The contribution of the physical mechanism in the adsorption process could also be recognized from the thermodynamic and D-R isotherm analysis. The ΔH° values for both metal ions were found to be <40 kJ mol^{-1} (Table 6), indicating that van der Waals force interaction mechanisms take place during the adsorption process. D–R isotherm model results reveal that the values of E_{ad} are <8 kJ mol^{-1} (Table 4), which confirms that the metal ions adsorption occurs through a physisorption process, applying van der Waals force.

In conclusion, the CoO/NiO@bio-char sorbent interacts with Zn(II) and Cd(II) ions through both physisorption and chemisorption (multiple mechanisms), depending on the adsorption phase. The pseudo-second-order kinetic model suggests an interaction-driven process, where electrostatic forces and possible surface complexation contribute to adsorption kinetics. However, thermodynamic parameters indicate that the overall process is governed by physisorption, as suggested by the relatively low activation energy (E_a) and enthalpy change (ΔH). This dual-mode behavior is common in biochar-based adsorbents, where fast kinetics (resembling chemisorption) and low binding energies (indicative of physisorption) coexist. This suggests that initial metal ion uptake is rapid and controlled by electrostatic attractions, potentially involving outer-sphere complexation or hydrogen bonding. However, as equilibrium is approached, weak physisorption forces dominate, resulting in an adsorption process that is primarily physical in nature rather than chemically irreversible. The proposed sorption mechanisms are illustrated in Fig. 12. The same mechanisms have been observed in the adsorption of Zn(II), and Cd(II) ions using potato starch phosphate (PSP) polymer,[2] Wood ash amended bio-char,[8] $KMnO_4$/hematite modified corn straw bio-char (MnFeB),[9] multi-walled carbon nanotubes,[10] $KMnO_4$-activated spinach waste bio-char,[16] Chitosan-modified MXene (CSMX),[37] and Magnesium/coconuts shell activated carbon composite (Mg-AC).[51]

3.3. Desorption and recycling investigation

Investigating the desorption and reusability of CoO/NiO@bio-char is essential to assess its practicality and sustainability as an adsorbent. This study evaluated the efficiency of different acidic solutions—sulfuric acid, hydrochloric acid, and nitric acid at a concentration of 1.0 M—for desorbing Zn(II) and Cd(II) ions from the loaded sorbent. Experimental parameters were maintained at a sorbent dose of 3.0 g L^{-1}, shaking time of 240 minutes, and room temperature. The results, illustrated in

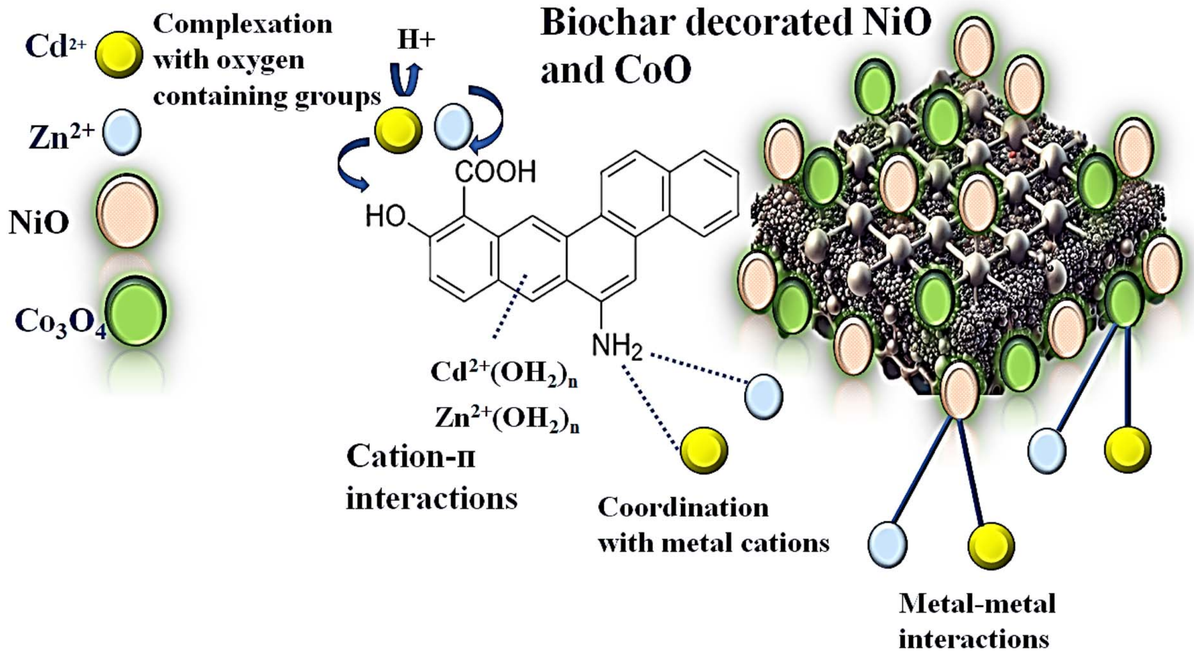

Fig. 12 The proposed sorption mechanisms for Zn(II), and Cd(II) ions on CoO/NiO@bio-char sorbent.

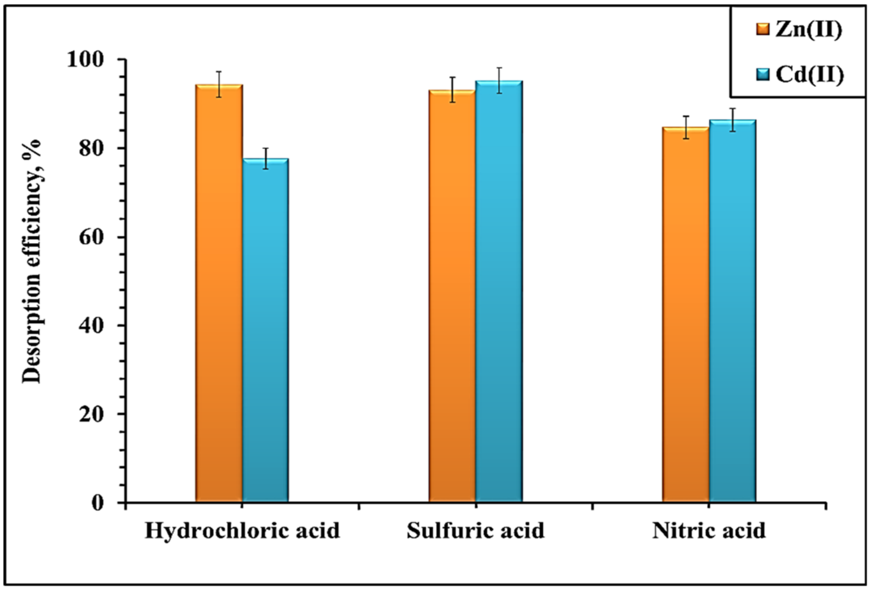

Fig. 13 Zn(II), and Cd(II) desorption from loaded CoO/NiO@bio-char sorbent using different solutions (3.0 g L^{-1}, room temperature; 240 min).

Fig. 13, revealed that all acidic solutions facilitated desorption, with sulfuric acid emerging as the most effective eluent, achieving elution yields of 95.2% for Zn(II) and 93.1% for Cd(II). The superior performance of sulfuric acid may be attributed to its ability to effectively disrupt metal-sorbent interactions, making it a viable candidate for industrial applications.

The recycling performance of CoO/NiO@bio-char was further examined across five successive sorption-desorption cycles, as summarized in Table S4.† The CoO/NiO@biochar composite demonstrated high regeneration efficiency, maintaining an average adsorption efficiency of 80.8% for Zn(II) and 63.6% for Cd(II) across five cycles. The desorption efficiency remained stable at >90% using sulfuric acid as an eluent. While a slight decrease in adsorption capacity (~5%) was noted, this is within an acceptable range for industrial applications. The minimal change in adsorption and desorption efficiencies confirms the structural stability of the composite, indicating that the active phase remains intact even after multiple cycles. These findings highlight the CoO/NiO@bio-char composite's resilience and efficiency in heavy metal ion recovery, aligning with the global demand for sustainable and reusable materials in wastewater treatment. By demonstrating high performance across multiple cycles, this material proves to be a promising candidate for scalable and environmentally friendly remediation technologies.

4. Conclusion

The synthesis of CoO/NiO@bio-char composites *via* pyrolysis and ultrasonic-assisted methods represents a significant advancement in sustainable materials for environmental applications. This study has demonstrated that the novel composite exhibits superior adsorption capabilities for Zn(II) and Cd(II) ions, achieving maximum adsorption capacities of 18.9 mg g^{-1} and 10.2 mg g^{-1}, respectively. Comprehensive analyses have validated that the adsorption mechanism is primarily governed by chemisorption, supported by electrostatic interactions, surface complexation, and intra-particle diffusion mechanisms. Additionally, thermodynamic investigations confirmed the endothermic, spontaneous, and energetically favorable nature of the adsorption process. The findings underscore the potential of combining renewable biomass with innovative synthesis techniques to produce efficient adsorbents, aligning with the principles of green chemistry. The developed composite not only exhibited high reusability over multiple sorption-desorption cycles but also demonstrated scalability and versatility for practical wastewater remediation applications. This reflects that the present work contributes valuable insights into the design of functional materials for addressing pressing environmental challenges. The integration of sustainable practices and advanced material science in this study offers a promising pathway for the development of next-generation adsorbents, paving the way for cleaner water resources and a healthier environment.

Data availability

The data supporting the findings of this study are available from the corresponding author upon reasonable request. This includes: raw data: experimental results, adsorption isotherm data, kinetic profiles, thermodynamic evaluations, and characterization outputs (*e.g.*, FTIR, XRD, SEM-EDX, Raman spectroscopy). Processed data: tabulated data used for analysis and graphical representations in the manuscript.

Author contributions

Walaa Gado: materials characterization and data curation. Asmaa Morshedy: material synthesis. Ahmed Masoud: methodology, experimental studies, data interpretation. Ard elshifa

Mohammed: data curation & interpretation and editing manuscript. Entsar Taha: data curation & interpretation. Adel El-Zahhar: validation, data interpretation, reviewing the original draft. Majed Alghamdi: validation, data curation, reviewing the original draft. Ahmed El Naggar: data curation & interpretation, writing & editing the manuscript, Esraa El-Fawal: data curation & interpretation and taking part in writing/editing the manuscript.

Conflicts of interest

The authors declare no conflict of interest.

Acknowledgements

The authors extend their appreciation to the Deanship of Research and Graduate Studies at King Khalid University for funding this work through Large Research Project under grant number RGP 2/74/45.

References

1 V. K. Gupta, A. Nayak, B. Bhushan and S. Agarwal, *Crit. Rev. Environ. Sci. Technol.*, 2015, **45**, 613–668.

2 V. K. Gupta, M. R. Ganjali, A. Nayak, B. Bhushan and S. Agarwal, *Chem. Eng. J.*, 2012, **197**, 330–342.

3 A. G. El-Said, N. A. Badawy and S. E. Garamon, *Environ. Anal. Toxicol.*, 2018, **8**, 1–5.

4 S. Lal, P. Singh, A. Singhal, S. Kumar, A. P. Singh Gahlot, N. Gandhi and P. Kumari, *RSC Adv.*, 2024, **14**, 3413–3446.

5 A. Nayak, B. Bhushan, V. Gupta and L. Rodriguez-Turienzo, *J. Environ. Chem. Eng.*, 2016, **4**, 4342–4353.

6 S. H. Peng, R. Wang, L. Z. Yang, L. He, X. He and X. Liu, *Ecotoxicol. Environ. Saf.*, 2018, **165**, 61–69.

7 M. Dardouri, F. Ammari, A. BelHadj Amor and F. Meganem, *Mater. Chem. Phys.*, 2018, **216**, 435–445.

8 S. Cairns, S. Chaudhuri, G. Sigmund, I. Robertson, N. Hawkins, T. Dunlop and T. Hofmann, *Environ. Technol. Innov.*, 2021, **24**, 101961.

9 X. Kang, N. Geng, Y. Li, X. Li, J. Yu, S. Gao, H. Wang, H. Pan, Q. Yang, Y. Zhuge and Y. Lou, *Bioresour. Technol.*, 2022, **363**, 127817.

10 M. A. Salam, G. Al-Zhrani and S. A. Kosa, *C. R. Chim.*, 2012, **15**, 398–408.

11 M. C. Benalia, L. Youcef, M. G. Bouaziz, S. Achour and H. Menasra, *Arab. J. Sci. Eng.*, 2022, **47**, 5587–5599.

12 Z. J. Fu, S. K. Jiang, X. Y. Chao, C. X. Zhang, Q. Shi, Z. Y. Wang, M. L. Liu and S. P. Sun, *Water Res.*, 2022, **222**, 118888.

13 J. Jayaraman, J. Kumaraswamy, Y. K. S. S. Rao, M. Karthick, S. Baskar, M. Anish, A. Sharma, A. S. Yadav, T. Alam and M. I. Ammarullah, *RSC Adv.*, 2024, **14**, 34769–34790.

14 M. Y. Alyapyshev, V. A. Babain, Y. A. Ustynyuk, W.-S. Chen, W.-C. Liang, C.-H. Lee, C. Chen, T. Xu, Y. Li, L. Yang, Z. Xu and Q. Sun, *IOP Conf. Ser.:Mater. Sci. Eng.*, 2017, **167**, 012005.

15 K. H. Hama Aziz, F. S. Mustafa, K. M. Omer, S. Hama, R. F. Hamarawf and K. O. Rahman, *RSC Adv.*, 2023, **13**, 17595–17610.

16 A. Nayak, B. Bhushan, V. Gupta and P. Sharma, *J. Colloid Interface Sci.*, 2017, **493**, 228–240.

17 A. Ben Bouabdallah and N.-E. Djelali, *Rev. Roum. Chim.*, 2015, **60**, 321–330.

18 V. C. Srivastava, I. D. Mall and I. M. Mishra, *Colloids Surf., A*, 2008, **312**, 172–184.

19 W. Jing, C. Yang, X. Lin, M. Tang, D. Lian, Y. Yu and D. Liu, *RSC Adv.*, 2024, **14**, 39995–40005.

20 B. Wang, J. Lan, C. Bo, B. Gong and J. Ou, *RSC Adv.*, 2023, **13**, 4275–4302.

21 V. K. Gupta and A. Nayak, *Chem. Eng. J.*, 2012, **180**, 81–90.

22 M. Ngabura, S. A. Hussain, W. A. W. A. Ghani, M. S. Jami and Y. P. Tan, *J. Environ. Chem. Eng.*, 2018, **6**, 2528–2539.

23 M. A. Moniem, A. M. A. El Naggar, H. A. El Sayed, M. S. Mostafa, N. M. Khalil and M. E. D. Hassan, *Egypt. J. Pet.*, 2018, **27**, 991–995.

24 M. M. Ali, S. A. Abedelmaksoud, M. H. Taha, A. M. A. El Naggar, A. S. Morshedy and A. A. Elzoghbi, *Radiochemistry*, 2020, **62**, 204–215.

25 Q. Hu, S. Pang and D. Wang, *Sep. Purif. Rev.*, 2022, **51**, 281–299.

26 J. P. Vareda, *J. Mol. Liq.*, 2023, **376**, 121416.

27 J. Wang and X. Guo, *Crit. Rev. Environ. Sci. Technol.*, 2023, **53**, 1837–1865.

28 Y. Wang, C. Wang, X. Huang, Q. Zhang, T. Wang and X. Guo, *Chemosphere*, 2024, **349**, 140736.

29 M. Mozaffari Majd, V. Kordzadeh-Kermani, V. Ghalandari, A. Askari and M. Sillanpää, *Sci. Total Environ.*, 2022, **812**, 151334.

30 M. A. Al-Ghouti and D. A. Da'ana, *J. Hazard. Mater.*, 2020, **393**, 122383.

31 T. A. Saleh, *Interface Sci. Technol.*, 2022, **34**, 65–97.

32 A. N. Ebelegi, N. Ayawei, D. Wankasi, A. N. Ebelegi, N. Ayawei and D. Wankasi, *Open J. Phys. Chem.*, 2020, **10**, 166–182.

33 J. Song, Z. Huang and M. Gamal El-Din, *Chem. Eng. J.*, 2021, **421**, 129937.

34 D. R. Abd El-Hafiz, S. A. El-Temtamy, M. A. Ebiad, R. A. El-Salamony, S. A. Ghoniem, A. M. A. El Naggar and T. S. Gendy, *Int. J. Hydrogen Energy*, 2020, **45**, 9783–9794.

35 A. F. Abou-Hadid, U. A. El-Behairy, M. M. Elmalih, E. Amdeha, A. M. A. El Naggar, M. H. Taha and A. E. M. Hussein, *Biomass Convers. Biorefin.*, 2022, **14**, 10501–10516.

36 T. Golgoli, K. Ghanemi and F. Buazar, *J. Mol. Liq.*, 2024, **393**, 123680.

37 N. R. Azeez, S. S. Salih, M. Kadhom, H. N. Mohammed and T. K. Ghosh, *Green Chem. Eng.*, 2024, **5**, 339–347.

38 B. R. Venkata, *J. Appl. Sci.*, 2014, **14**(13), 1372–1378.

39 R. Karthik and S. Meenakshi, *Int. J. Biol. Macromol.*, 2015, **78**, 157–164.

40 Y. Hu, X. Wang, Y. Zou, T. Wen, X. Wang, A. Alsaedi, T. Hayat and X. Wang, *Chem. Eng. J.*, 2017, **316**, 419–428.

41 A. S. Morshedy, M. H. Taha, D. M. Abd El-Aty, A. Bakry and A. M. A. El Naggar, *Environ. Technol. Innov.*, 2021, **21**, 101363.

42 J. Liao, T. Xiong, L. Ding, Y. Xie, Y. Zhang and W. Zhu, *Biochar*, 2022, **4**, 1–18.

43 P. T. Tho, H. T. Van, L. H. Nguyen, T. K. Hoang, T. N. Ha Tran, T. T. Nguyen, T. B. Hanh Nguyen, V. Q. Nguyen, H. Le Sy, V. N. Thai, Q. B. Tran, S. M. Sadeghzadeh, R. Asadpour and P. Q. Thang, *RSC Adv.*, 2021, **11**, 18881–18897.

44 J. C. Igwe and A. Augustine, *Eclét. Quím.*, 2007, **32**, 33–42.

45 M. T. Mihajlović, S. S. Lazarević, I. M. Janković-Častvan, B. M. Jokić, D. T. Janaćković and R. D. Petrović, *Chem. Ind. Chem. Eng. Q.*, 2014, **20**, 283–293.

46 M. J. Page, K. Soldenhoff and M. D. Ogden, *Hydrometallurgy*, 2017, **169**, 275–281.

47 I. Persson, *Pure Appl. Chem.*, 2010, **82**, 1901–1917.

48 F. I. Khalili, N. H. Salameh and M. M. Shaybe, *J. Chem.*, 2013, **2013**, 586136.

49 H. Demey, T. Vincent and E. Guibal, *Chem. Eng. J.*, 2018, **332**, 582–595.

50 A. Andelescu, M. A. Nistor, S. G. Muntean and M. E. Rădulescu-Grad, *Sep. Sci. Technol.*, 2018, **53**, 2352–2364.

51 H. Yanagisawa, Y. Matsumoto and M. Machida, *Appl. Surf. Sci.*, 2010, **256**, 1619–1623.